

Trade-off between complexity and energy in quantum phase estimation

Yukuan Tao,^{*} Mădălin Guță,[†] and Gerardo Adesso[‡]

*School of Mathematical Sciences and Centre for the Mathematics and Theoretical Physics of Quantum Non-Equilibrium Systems,
University of Nottingham, University Park, Nottingham NG7 2RD, UK*

Quantifying the energetic cost of implementing quantum operations is essential for assessing the efficiency and scalability of quantum sensing and information-processing technologies. Here, we introduce a framework for analysing the interplay between complexity and energy cost of quantum processes. In particular, we apply our framework to a sequential quantum phase estimation protocol, where a phase of physical significance is encoded in a quantum channel. The channel is applied to a probe state repeatedly until the probe is measured and the outcome leads to an estimate on the phase. We establish a trade-off relation between the total energy cost of the protocol and the number of times the channel is applied (complexity), while reaching a desired estimation precision. A sweet spot is located where the two quantities are co-optimised. The principles of our analysis can be adapted to benchmark the energetic requirements in other quantum protocols and devices.

I. INTRODUCTION

Quantum protocols are known to outperform their classical counterparts for various tasks. This so-called *quantum advantage* relies on different characteristics which are available in the quantum realm, such as coherent superpositions [1] and entanglement of quantum states [2, 3]. Identifying and characterising the *resources* enabling quantum advantages is a major goal of quantum information science, often studied under the umbrella of quantum resource theory [4]. The advantage itself may manifest in a variety of forms and can be quantified by means of different figures of merit, depending on the task at hand. In particular, by quantum advantage in *complexity* we mean that, while reaching the same goal, the total number of elementary operations performed by a quantum protocol is smaller than that by a classical one. For examples, in quantum computation [5, 6], Grover’s algorithm [7] achieves a quadratic speed-up for the searching problem, and, more remarkably, Shor’s algorithm [8] is able to attain an exponential speed-up for integer factorisation. Both are relevant to important computational fields such as cryptography [9]. Exponential speed-up is also possible for Hamiltonian simulation [10, 11] – following from the idea of simulating physical systems through quantum computers as originally raised by Feynman [12]. Meanwhile, in quantum metrology, there exists a quadratic speed-up to reach the desired estimation precision, termed the Heisenberg limit [13–15]. This can help improve performance in a wide range of applications, including gravitational sensing [16], biological imaging [17] and timing [18].

Despite their promises, the above quantum advantages typically only hold under a noise-free setting. In realistic experimental situations, the target system inevitably interacts with its surrounding, being the experimental device or the inaccessible environment, causing decoherence on its evolution [19]. The resulting noisy quantum operation deviates from the desired one and the *implementation error* generally leads to a larger complexity, sometimes even losing the quantum advantage: under commonly encountered noise models, Refs. [20–22] and Ref. [23] show that Grover’s algorithm and Shor’s algorithm, respectively, can only attain partial complexity advantage if the noise is weak enough, while Refs. [24–26] indicate that the

metrological advantage is reduced to a constant factor unless specific structures of the noise are assumed.

In order to retain the ideal quantum complexity, various error mitigation techniques have been designed [24–31], and the resulting Noisy Intermediate-Scale Quantum (NISQ) technologies [32] represent the state-of-the-art progress made towards commercialisation. Generally, to reduce the implementation error we can increase the power of the coupled device, or exert external controls to detect and correct the noise. Either way, complexity reduction comes with extra energy cost and a competition takes place between a smaller number of operations and larger energy cost per operation. In Refs. [33–35] the *total energy cost* of quantum protocols is treated as another important quantity that one wants to optimise for both scientific interest and near term realisation. From this perspective, since the optimal complexity – corresponding to zero implementation error – can be expensive, some finite error may indeed be preferred for an energy optimisation task.

Motivated by the quest to explore more concretely the aforementioned trade-off between complexity and energy cost, in this work we study the balance between the two in the context of *quantum metrology*. A typical metrological task consists of a pair $(\mathcal{G}_\phi, \text{Strat})$, where \mathcal{G}_ϕ is an operation that encodes the parameter ϕ to be estimated and *Strat* refers to strategies adopted to extract the parameter. The complexity here is represented by the number of times \mathcal{G}_ϕ is queried. A strategy consists of three main components: state preparation, intermediate controls (including error mitigation procedures) and measurements. Refs. [36–39] have studied the cost of these components, while in most cases \mathcal{G}_ϕ is assumed to be the result of a free evolution and so does not incur additional cost. In this work we will introduce scenarios where energy is required to initiate the evolution. The form of \mathcal{G}_ϕ then depends on its implementation energy, and the larger this cost, the smaller the number of iterations of \mathcal{G}_ϕ is required to reach a desired estimation precision, leading to a complexity-energy trade-off relation. The corresponding implementation error is quantified by a distance between \mathcal{G}_ϕ and its ideal form. The main finding of this work exposes a critical error level for complexity-energy co-optimisation, beyond which the saving in one factor is overwhelmed by the overhead in the other. We also expect that the

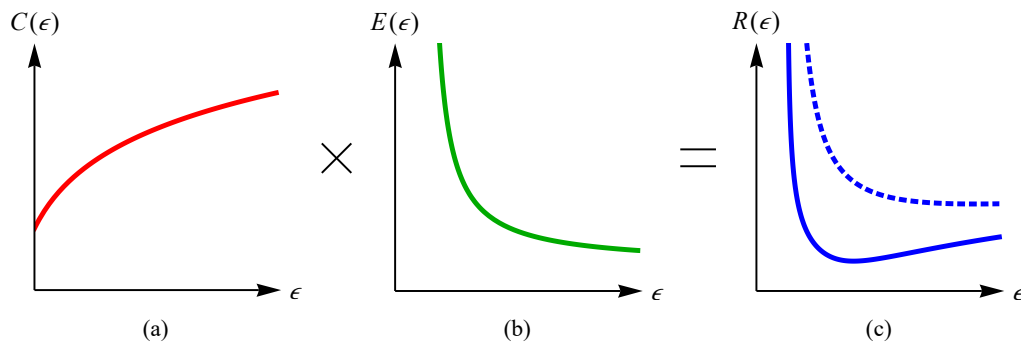


FIG. 1. A qualitative plot of the key variables characterising a quantum protocol as in Eq. (3). Here ϵ is a generic quantifier for the implementation error of each elementary unitary gate, with $\epsilon \rightarrow 0$ corresponding to the ideal limit of perfect implementation. Competition takes place between (a) growing gate complexity $C(\epsilon)$ and (b) decreasing energy cost $E(\epsilon)$ per gate as ϵ increases. (c) The resulting total energy cost $R(\epsilon)$ may (solid curve) or may not (dashed curve) have a global minimum at finite ϵ .

combination of our results and the established complementary ones can lead to a more complete energy benchmarking in quantum sensing and metrology protocols.

The overall flow of the paper is as follows: Section II introduces the key concepts behind the trade-off relation that are expected to apply qualitatively to all relevant protocols, Section III describes the basics of the quantum phase estimation protocol in metrology and its connection with the trade-off framework, while Section IV dives deeper into this connection by quantitatively analysing a full sequential phase estimation protocol carried out on an optical platform, and drawing general insights on the interplay between complexity and energy cost in quantum processes. The paper is concluded by a summary and outlook in Section V.

II. THE TRADE-OFF FRAMEWORK

Let us begin with a qualitative description of the origin of the trade-off. Suppose we have a fixed objective and a protocol to reach it. The protocol takes energy to be implemented and involves a certain notion of complexity. Both can depend on various factors, with the implementation quality being the focus of this work. In general, the better the protocol is implemented, the objective can be achieved with a smaller complexity, but at the expense of a larger energy cost. The optimal quality level can be determined accordingly.

To formalise the notion of complexity clearly, we focus on quantum tasks with the following ideal structure:

$$\rho_0 \xrightarrow{U^N} \rho_N \quad (\times Q_N). \quad (1)$$

In words, an input state ρ_0 undergoes a sequence of N identical unitary transformations U . Desired information accumulates in the final state ρ_N and is often extracted through classical post-processing of measurement results. The whole sequence is repeated independently for Q_N rounds in order to gain a set amount of total information. This set goal can be represented by a fixed constraint, denoted as Con , whose exact form depends on the task. The total number of gates implemented is

$Q_N \cdot N$ and optimising over N with respect to the fixed goal gives the (gate) *complexity* C of the protocol:

$$C := \min_N (Q_N \cdot N) |_{Con}. \quad (2)$$

Denote E as the *energy cost* for constructing each U -block. The *total energy cost* is then $R = C \times E$. However, perfect implementation can be affected by both experimental and fundamental limitations. The actual implemented gates will not be unitary in general and an error dependence needs to be added to the quantities defined so far:

$$R(\epsilon) = C(\epsilon) \times E(\epsilon), \quad (3)$$

where ϵ is some error parameter quantifying deviation from the desired unitary gate. A larger error (i.e., lower implementation quality) tends to increase the complexity, as intuitively less information is encoded in each implemented gate, while reducing the energy cost per gate.

We are interested in scenarios where such a trade-off leads to an initially decreasing total energy cost $R(\epsilon)$ as a function of the error ϵ , as illustrated in Figure 1. Note that if ϵ — and hence $E(\epsilon)$ — is fixed, the total energy cost becomes equivalent to the gate complexity as a resource quantifier. It is thus precisely through the dynamic interplay between the two, as mediated by a variable implementation error, that we can introduce a novel resource analysis on the quantum protocol at hand. In particular, minimising the complexity is not equivalent to minimising the total energy cost $R(\epsilon)$ with respect to ϵ . We also emphasise that the objective here is on optimising the quantum protocol itself, rather than determining if a quantum over classical energetic advantage exists; for works on the latter, we refer to Refs. [40–42].

For a similar purpose to ours (see also the earlier analysis in Ref. [37]), Ref. [33] brings up the necessity to build a framework within which costs of quantum protocols can be analysed and compared in a universal fashion. The proposed framework is dubbed Metric-Noise-Resource (MNR) [34]: a metric is chosen to assess the performance, the effect of noise is taken into account, and the total resource cost is evaluated.

A notion of efficiency is correspondingly defined as

$$\text{Efficiency } \eta = \frac{\text{Metric}}{\text{Resource}}. \quad (4)$$

For us, the constraint can be quantified by a suitably chosen metric, on which both resource cost (taken to be energy here) and complexity depend. Then for a fixed constraint, or equivalently a target value of the metric, we can minimise the total energy cost over ϵ to determine the optimal energy efficiency η . We shall return to this connection at the end of Section IV, where the energy analysis is carried out for a quantum phase estimation protocol performed on an optical platform, with the quantum Fisher information acting as the metric.

III. QUANTUM PHASE ESTIMATION

A. Quantum Fisher Information and Complexity

A quantum metrology task can often be recast in the form of quantum phase estimation (QPE). In general, a phase ϕ is encoded in some quantum operations which are applied to a probe state and by measuring the probe we can obtain an estimate on the phase. The precision of the estimation can be quantified by the quantum Fisher information (QFI), which captures geometrically the rate of change of the probe state under an infinitesimal variation of the phase parameter [43]. To compute the QFI, we first introduce the classical Fisher information (CFI): for a positive operator-valued measurement (POVM) defined by the set of operators $\mathbf{M} = \{M_i\}$ and a probe state ρ_ϕ parametrised by the phase ϕ , the CFI is

$$F_c[\mathbf{M}](\phi) = \sum_i \text{Tr}(\rho_\phi M_i) l_i^2, \quad (5)$$

$$l_i = \partial_\phi \log \text{Tr}(\rho_\phi M_i) = \frac{\text{Tr}(\dot{\rho}_\phi M_i)}{\text{Tr}(\rho_\phi M_i)},$$

where the dot denotes the derivative over ϕ .

The QFI is achieved by optimising the CFI over all possible POVMs:

$$F_q(\phi) = \max_{\mathbf{M}} F_c[\mathbf{M}](\phi).$$

It turns out the optimal \mathbf{M} are projectors onto the eigenspaces of the symmetric logarithmic derivative (SLD) operator Λ_ϕ , which satisfies the equation $\partial_\phi \rho_\phi = \frac{1}{2}(\Lambda_\phi \rho_\phi + \rho_\phi \Lambda_\phi)$. Suppose the same procedure is repeated independently for Q times, by the additive nature of the QFI for product states [44], the total QFI becomes $QF_q(\phi)$, and the quantum Cramér–Rao bound [45] states that

$$\text{Var}[\hat{\phi}] \geq \frac{1}{QF_q(\phi)}, \quad (6)$$

where $\hat{\phi}$ is an unbiased estimator of ϕ based on the Q measurement outcomes and $\text{Var}[\hat{\phi}]$ is its variance. Note that the bound

is only achievable in the asymptotic limit of large $Q \gg 1$ by employing adaptive estimation procedures for determining the optimal measurement [46].

Within this framework we study the sequential strategy of the type described in Eq. (1) as inspired by Refs. [47–49]: the phase ϕ is ideally imprinted via a unitary phase shift operator $\exp(-i\phi H/2)$ where H is a control Hamiltonian. The operator functions as an oracle and each time we make a query it is repeatedly applied to the probe state, which will carry accumulating information about the phase. Finally the state is measured, yielding an estimate on the phase. If the oracle is applied N times, we denote the QFI of the final state by F_N . In the rest of this work we will treat $N \geq 1$ as a continuous variable for simplicity [49, 50].

To determine the complexity, we quantify Con in Eq. (2) by demanding a target value, denoted as δ^2 , of the quantity on the right hand side of (6), so that δ^2 lower bounds the estimator variance. Naively, the number of independent repetitions of an N -step sequence needed to reach the set goal is

$$q_N = \frac{1}{\delta^2 \cdot F_N}, \quad (7)$$

and so the complexity can be derived as

$$c = \min_N (q_N \cdot N) \Big|_{\delta^2}$$

$$= \frac{1}{\delta^2} \cdot \min_N \frac{N}{F_N} \quad (8)$$

$$= \frac{1}{\delta^2} \cdot \frac{N_{\text{opt}}}{F_{N_{\text{opt}}}},$$

where N_{opt} is the optimal step for the minimisation and $|_{\delta^2}$ is a shorthand for the constraint $|[QF_q(\phi)]^{-1} \leq \delta^2$.

However, Eq. (8) must be taken with a pinch of salt, and c will be referred to as the *raw complexity*; the discrepancy arises due to the fact that q_N as calculated by Eq. (7) is not necessarily an integer and hence implicitly assumes F_N to be linear over N , while Q in (6) is an integer. In Appendix A we elaborate on the general behaviour of F_N and how its nonlinearity calls for a correction to c . To address this discrepancy, the *true complexity* of the QPE protocol will be determined as follows.

Suppose an N -step sequence is first repeated fully for $Q_N = \lfloor q_N \rfloor$ times, $\lfloor q_N \rfloor$ being the integer part of q_N , followed by a final sequence with $N_0 \leq N$ steps. By additivity of the QFI, the overall QFI from the $(Q_N + 1)$ sequences is $Q_N F_N + F_{N_0}$. Thus, to meet the constraint set by δ^2 , N_0 must be such that

$$F_{N_0} = \frac{1}{\delta^2} - Q_N F_N. \quad (9)$$

The true complexity is then given by

$$C = \min_N (NQ_N + N_0) \Big|_{\delta^2}. \quad (10)$$

The minimisation will be computed numerically and the minimal point is anticipated to be near $N \approx N_{\text{opt}}$. As seen shortly and qualitatively explained in Appendix A, the true complexity can be well approximated by the raw one when the implementation error is large enough.

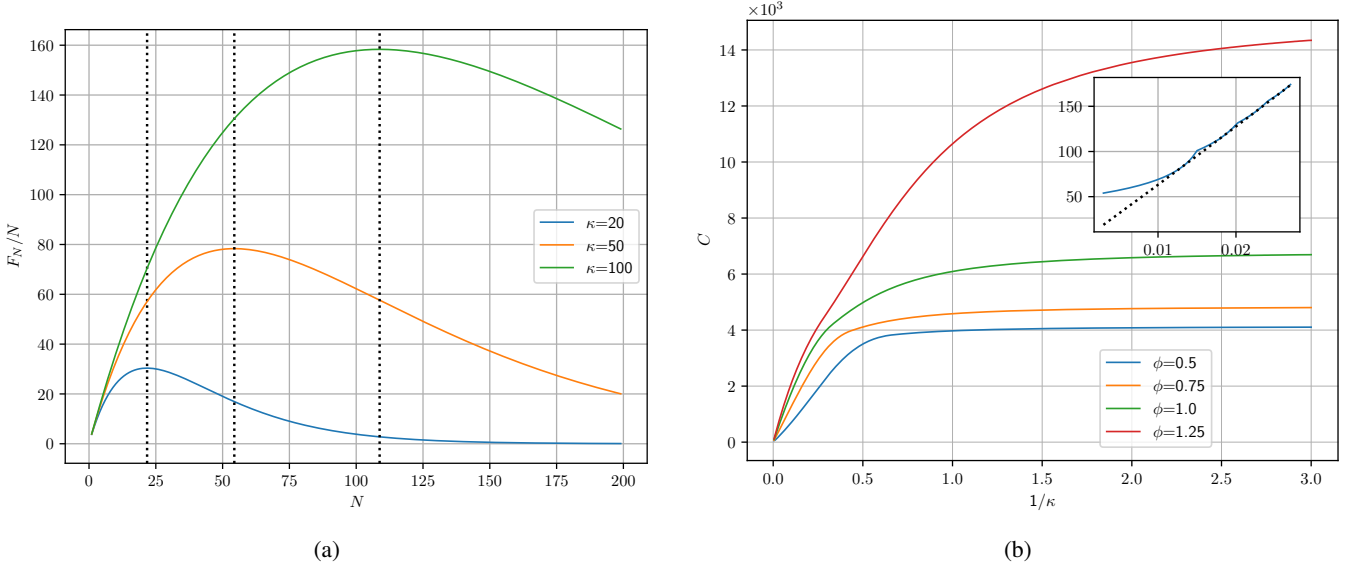


FIG. 2. (a) Plots of the ratio between the QFI and the steps number, F_N/N , for different values of the concentration parameter of the von Mises-Fisher distribution κ and a fixed phase $\phi = 0.5$ to be estimated. Observe the non-monotonic behaviour predicted by Eq. (14): the ratio grows linearly with N first, reaches its maximum and decays exponentially afterwards. As indicated by the vertical dotted lines, the optimal step N_{opt} is well approximated by $-[2 \log(\lambda_{\perp})]^{-1}$; (b) The resulting complexity (10) is plotted against $1/\kappa$ (representing the implementation error ϵ) for the desired lower bound on the estimator variance, $\delta^2 = 10^{-4}$, implied by Eq. (6). Observe the growing pattern as anticipated by Figure 1(a). The inset exhibits the zoom-in at small $1/\kappa$ for $\phi = 0.25$. Each teeth of the zigzag pattern corresponds to a region that applies the same number of complete sequences Q_N . The dotted line corresponds to the raw complexity computed by Eq. (8). Notice that the raw complexity vanishes in the ideal limit, and approximates the true complexity better as $1/\kappa$ grows, as discussed in Appendix A.

B. Modelling the Gate Implementation Error

To incorporate the implementation error, we assume that the (ideally unitary) quantum channels imprinting the phase in each round of the QPE protocol are in fact generated by a random Hamiltonian. For a qubit system, this amounts to taking $H_{\mathbf{n}} = \mathbf{n} \cdot \boldsymbol{\sigma}$, where \mathbf{n} is a unit Bloch vector sampled from some probability distribution $p(\mathbf{n})$ and $\boldsymbol{\sigma}$ is the vector of Pauli operators. In the ideal limit, $p(\mathbf{n})$ is a Dirac delta function at \mathbf{n}_0 , where \mathbf{n}_0 is the Bloch vector of the desired control Hamiltonian H . Both the error and the QFI, $F_N \equiv F_N(p; \phi)$, depend on the distribution. We will use semicolon to separate free parameters that affect the implementation error. The resulting noisy gate (channel) is

$$\mathcal{G}_{p;\phi}(\cdot) = \int_{|\mathbf{n}|=1} e^{-i\phi\mathbf{n}\cdot\boldsymbol{\sigma}/2}(\cdot)e^{i\phi\mathbf{n}\cdot\boldsymbol{\sigma}/2}p(\mathbf{n})d\mathbf{n}. \quad (11)$$

Correspondingly, the channel performs random rotation on the Bloch sphere. Let \mathbf{s} be the Bloch vector of the probe qubit. It is transformed by the implemented gate as

$$\mathbf{s} \rightarrow \mathbf{G}_{p;\phi} \mathbf{s}, \quad \mathbf{G}_{p;\phi} = \int_{|\mathbf{n}|=1} \mathbf{R}_{\mathbf{n}}(\phi)p(\mathbf{n})d\mathbf{n}, \quad (12)$$

where $\mathbf{R}_{\mathbf{n}}(\phi)$ represents the rotation around \mathbf{n} by an angle ϕ .

C. Computing Complexity: An Example

As an example of the model introduced in the previous two subsections, we first consider the following setup, studied by Ref. [48]. The initial state is set to be $\rho_0 = |\psi_0\rangle\langle\psi_0|$, $|\psi_0\rangle = (|0\rangle + |1\rangle)/\sqrt{2}$ and the desired Hamiltonian is $H = \sigma_z$. The random Bloch vector is sampled from the von Mises-Fisher distribution [51], $p_{\kappa}(\theta) = \frac{\kappa e^{\kappa \cos \theta}}{4\pi \sinh \kappa}$, where θ is the azimuthal angle, and κ is the concentration parameter. $H_{\mathbf{n}}$ becomes uniformly distributed as $\kappa \rightarrow 0$, and is sharply peaked at σ_z as $\kappa \rightarrow \infty$. This distribution can be seen as the counterpart of a Gaussian over the Bloch sphere and the implementation error can be represented by $\epsilon \sim 1/\kappa$. Furthermore, since $p_{\kappa}(\theta)$ has axial symmetry around z , the resulting quantum channel is phase-covariant (commuting with σ_z) and the transformation matrix (12) can be expressed in the form of [52]

$$\mathbf{G}_{\kappa;\phi} = \begin{bmatrix} \lambda_{\perp}(\kappa; \phi) \cos \phi & -\lambda_{\perp}(\kappa; \phi) \sin \phi & 0 \\ \lambda_{\perp}(\kappa; \phi) \sin \phi & \lambda_{\perp}(\kappa; \phi) \cos \phi & 0 \\ 0 & 0 & \lambda_{\parallel}(\kappa; \phi) \end{bmatrix}. \quad (13)$$

Using the formula for $F_N(\kappa; \phi)$ derived in Appendix C of Ref. [48], we compute the complexity (10) and plot it in Figure 2(b). Note that the step that maximises the QFI is not $N_{\text{opt}}(\kappa; \phi)$ for the raw complexity (8): the quantity to be maximised here is F_N/N (plotted in Figure 2(a)) rather than F_N . The latter is shown to be well approximated by

$$F_N(\kappa; \phi) \approx N^2 \lambda_{\perp}^{2N-2} [\lambda_{\perp}^2 + (\partial_{\phi} \lambda_{\perp})^2], \quad (14)$$

so that F_N and F_N/N attain their maximum at around $-\lceil \log(\lambda_\perp) \rceil^{-1}$ and $N_{\text{opt}} = -\lceil 2 \log(\lambda_\perp) \rceil^{-1}$, respectively.

With the a priori probability distribution comes the lack of knowledge on physical details on how the phase-encoding channel is achieved. Consequently, only an educated guess can be made on the energy cost of the implementation. In the next Section, we restart with another more practical example and approach the QPE protocol from its physical foundation to realise a comprehensive resource analysis.

IV. CONSTRUCTION FROM FIRST PRINCIPLES

The detection of gravitational waves [53] represents one of the most significant developments in measurement science and technology. The detector uses powerful laser beams in an interferometric setup in order to detect gravitational waves causing minute relative displacements between mirrors placed at the end of each interferometer. The lasers constitute the dominant cost component of the QPE protocol, whose sensitivity is fundamentally constrained by sources of noise such as photon shot noise [54–56]. Consequently, achieving an optimal trade-off between energy cost and accuracy is crucial for maximising the efficiency of gravitational wave detection.

In this Section, we adopt the sequential procedure from Section III for a similar but simpler task: laser lights are shined on a target qubit instead; the two are coupled and the coupling strength can be encoded in a phase and hence estimated by the QPE protocol. This helps reveal information on physical details of the qubit, much as the phase difference that exposes the existence of gravitational waves. Due to the explicit physical origin, the energy cost of the phase shift operator can be readily evaluated, in contrast to the case in Section III C. The effect of the implementation error on the complexity is also derived. Combining both factors gives us the total energy cost of the estimation protocol. For completeness we also include the cost of state preparation and measurement that take place at the beginning and end of each sequence, respectively. Figure 7 at the end of this Section exhibits the overall circuit structure, while Table I below makes clear the meaning of each parameter to be defined in the following subsections.

Variable Parameters	
\bar{m}	number of photons spent per gate
δ^2	lower bound on the estimator variance as implied by (6)
M_s	number of cooling qubits per sequence during state preparation
M_m	number of cooling qubits per sequence during measurement
Fixed Parameters	
g	field-qubit coupling strength (the “phase” to be estimated)
T_0	temperature of the free qubits used for cooling
ω_0	transition frequency of the system qubit
ω_1	transition frequency of the pointer qubit
ω	frequency of the electromagnetic field

TABLE I. Summary of parameters relevant to our model.

A. Energy Bookkeeping

Before proceeding, we need to establish a consistent operational definition of energy cost, which will be applied throughout the remainder of the paper. Each building block of the QPE protocol can be described by an initial quantum state ρ of the system under consideration, assumed to be provided at no cost, followed by a target unitary operation V , after which only energy-conserving operations O are allowed (including unitary evolution, discarding subsystems, and measurements). The full QPE circuit is constructed through concatenation of such building blocks: the output quantum state of one block is treated as the free input state for the next one.

We define the energy cost of a block as the change in the system energy induced by V ,

$$E = \text{Tr}[H_0 (V\rho V^\dagger - \rho)], \quad (15)$$

where H_0 denotes the system’s Hamiltonian. This definition follows directly from energy conservation [57]: any change in the system energy must be supplied by an external energy storage device, referred to as a battery. Accordingly, E quantifies the energy exchanged with the battery per application of V .

Operationally, V can be realised by coupling the system to a battery state ρ_B via an energy-conserving joint unitary \tilde{V} satisfying $[\tilde{V}, H_B \otimes I_0 + I_B \otimes H_0] = 0$ (where H_B denotes the battery’s Hamiltonian), followed by decoupling [57–63]:

$$\text{Tr}_B[\tilde{V}(\rho_B \otimes \rho)\tilde{V}^\dagger] \approx V\rho V^\dagger. \quad (16)$$

Following [39, 57], we implicitly assume access to a battery with sufficiently large energy storage to implement all V operations across the protocol [64].

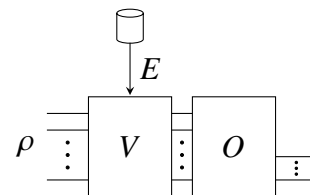


FIG. 3. An elementary building block used to quantify the energy cost: a free initial state ρ undergoes a non-energy-conserving unitary V , followed by energy-conserving operations collectively represented by O . The energy cost E is counted as the energy change of the state caused by V , supplied by a battery. The quantum output leg of O is treated as the initial state for the next elementary block.

We shall adopt the above as a bookkeeping convention throughout: different components of the protocol correspond to different choices of ρ and V , but the defining principle of E remains unchanged. Figure 3 illustrates this energy accounting, and Table II summarises the corresponding objects for each building block of the QPE protocol. This convention isolates the fundamental implementation cost associated with non-energy-conserving operations, leaving aside additional thermodynamic or hardware overheads. These are briefly considered in Appendix C for the protocol at hand.

Building block	ρ	V	O
Gate implementation	$\rho_N^{(S)} \otimes \rho_{\text{vac}}$	Displacement operator on the field	Field-qubit free evolution through the coupling (17) Discarding the post-evolution field state
State preparation	ρ_β	Cooling unitary	Discarding the auxiliary qubits
Measurement	$\rho_N^{(S)} \otimes 0\rangle\langle 0 ^{(P)}$	CNOT between system and pointer qubits	Measurement on the pointer qubit Discarding the probe qubit

TABLE II. Summary of the initial state ρ , the non-energy-conserving unitary operation V , and the subsequent energy-conserving operations O in each building block of the QPE protocol, as illustrated in Figure 3. Here S, P label the system probe qubit and pointer qubit, respectively, ρ_{vac} is the vacuum state of the EM field, and ρ_β is the thermal state of the cooling auxiliary qubits, as introduced in the following subsections.

B. Gate Implementation

Let the target system qubit (probe) be governed by the Hamiltonian $-\hbar\omega_0\sigma_z/2$, where ω_0 is the transition frequency of the two-level system. The qubit is coupled to a resonant monochromatic electromagnetic (EM) field of frequency ω ($\approx \omega_0$) travelling in the z -direction. Suppose the rotating wave approximation [65] holds, $|\omega_0 - \omega| \ll \omega_0 + \omega$. In the interaction picture, the system is then governed by a time-independent Hamiltonian [66, 67]:

$$H_S = \hbar g k_0 (E |1\rangle\langle 0| + E^* |0\rangle\langle 1|) = \hbar g k_0 E_0 (\mathbf{n} \cdot \boldsymbol{\sigma}), \quad (17)$$

where k_0 is a unit quantity (time^{-1}) to keep the coupling constant g dimensionless, $\mathbf{n} = [\cos \theta, \sin \theta, 0]^\top$ and $E = E_0 e^{i\theta}$ represents the amplitude E_0 and the phase θ of the field. Physically, the parameter g reflects the magnitude of the qubit dipole moment. To estimate it, we set the initial state to be $\rho_0 = |0\rangle\langle 0|$ and aim to implement the unitary gate

$$U_g = e^{-ig\sigma_x/2}.$$

Classically, this is achieved by tuning $\theta = 0$ and $2k_0 E_0 t = 1$, t being the total evolution time. Quantum fluctuation of the field, however, sets a fundamental limit on the implementation quality: semi-classically, E_0 and θ can be treated as random variables with means \bar{E}_0 and 0 , respectively, and the evolution time is $t = 1/(2k_0 \bar{E}_0)$. The gate implemented is then sampled from the set of unitary operators consisting of

$$e^{-iH_S t/\hbar} = \exp\left\{-ig \frac{E_0}{\bar{E}_0} \mathbf{n} \cdot \boldsymbol{\sigma}/2\right\} = \exp\left\{-ig \sqrt{\frac{m}{\bar{m}}} \mathbf{n} \cdot \boldsymbol{\sigma}/2\right\}, \quad (18)$$

where m is the (coherent) photon number of the EM field, treated as a random variable with mean \bar{m} . The ideal limit corresponds to $\bar{m} \rightarrow \infty$ when U_g is exactly applied to the qubit and the error may thus be characterised by $\epsilon \sim 1/\bar{m}$. For small \bar{m} , quantum statistics becomes significant and we have to resort to a full quantum treatment [68, 69], where random variables are further replaced with quantum operators.

Appendix B shows that in the semi-classical regime the QFI is well approximated by

$$F_N \equiv F_N(\bar{m}; g) \approx N^2 r^{2N}, \quad (19)$$

$$r \approx 1 - \frac{\Delta(g)}{2\bar{m}}, \quad \Delta(g) = \frac{g^2 + 1 - \cos(g)}{4},$$

provided $\bar{m} \gtrsim 100$, $g^2/\bar{m} \ll 1$ and the EM field is in its coherent state, representing lasers. Geometrically, the transformation on the yz plane of the Bloch sphere by the implemented channel (12) is reduced approximately to a rotation of angle g (corresponding to the desired unitary U_g) combined with a shrinking of factor r , matching the phase-covariant channel (13). The optimal step for the raw complexity (8) and the corresponding number of repetitions (7) are

$$N_{\text{opt}} \equiv N_{\text{opt}}(\bar{m}; g) = -\frac{1}{2 \log(r)} \approx -\frac{1}{2 \log\left(1 - \frac{\Delta(g)}{2\bar{m}}\right)} \approx \frac{\bar{m}}{\Delta(g)};$$

$$q_{N_{\text{opt}}} \equiv q_{N_{\text{opt}}}(\bar{m}; g, \delta^2) = \frac{1}{\delta^2 \cdot F_{N_{\text{opt}}}}$$

$$\approx \frac{1}{\delta^2} \cdot \left(\frac{\Delta(g)}{\bar{m}}\right)^2 \cdot \left(1 - \frac{\Delta(g)}{2\bar{m}}\right)^{-\frac{2\bar{m}}{\Delta(g)}} \approx \frac{e}{\delta^2} \cdot \left(\frac{\Delta(g)}{\bar{m}}\right)^2. \quad (20)$$

The raw complexity can be computed as

$$c(\bar{m}; g, \delta^2) = q_{N_{\text{opt}}} \cdot N_{\text{opt}} \approx \frac{e}{\delta^2} \cdot \frac{\Delta(g)}{\bar{m}}. \quad (21)$$

This is a good approximation of the true complexity (10), $C(\bar{m}; g, \delta^2)$, for large enough $1/\bar{m}$, as observed in the inset of Figure 4(a).

Moreover, we now hold knowledge on physical details of the implementation and hence its energy cost. To construct the N^{th} phase-encoding channel in a sequence, we follow the established procedure in Figure 3. As anticipated in Table II, the initial state ρ here is the tensor product of the probe state after the $(N-1)^{\text{th}}$ step and the vacuum state ρ_{vac} of the EM field, the non-energy-conserving unitary V is the displacement operator on the field that creates the coherent state of mean photon number \bar{m} , and the ensuing energy-conserving operations O consist of the free evolution through the field-qubit coupling (17) followed by a complete discarding of the field state at the end of the evolution. The output probe state then acts as part of the free initial state for the $(N+1)^{\text{th}}$ step, or as the pre-measurement state in the final step. The energy cost of the displacement operator, as computed by Eq. (15), is the energy difference between the vacuum and the coherent state, namely $\bar{m}\hbar\omega$. For convenience, we will set the photonic energy to be unit, $\hbar\omega = 1$, and so $E(\bar{m}) = \bar{m} \sim 1/\epsilon$. The total energy cost (3) is then

$$R \equiv R(\bar{m}; g, \delta^2) = C(\bar{m}; g, \delta^2) \cdot \bar{m}. \quad (22)$$

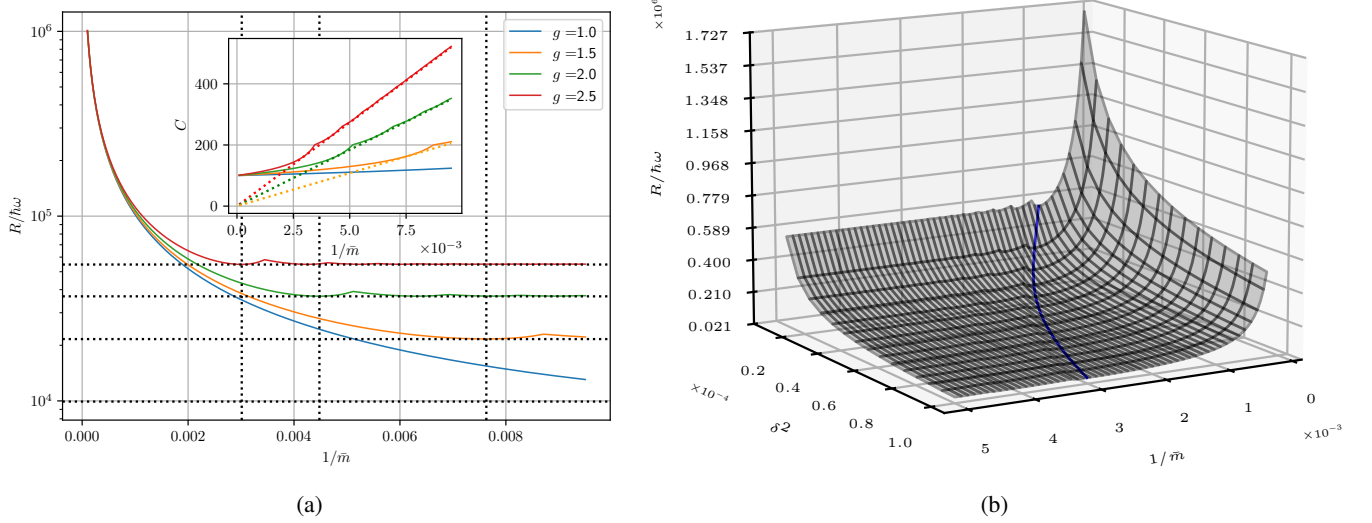


FIG. 4. (a) Plots of the total energy cost R (22), with the desired lower bound on the estimator variance set to $\delta^2 = 10^{-4}$, and the implementation error ϵ represented by $1/\bar{m}$, i.e., the inverse of the number of photons spent on implementing each phase-encoding gate. As reflected by the y-axis label, R is computed in units of the photonic energy of the EM field, $\hbar\omega$, and so numerically equals the total number of photons spent in implementing all the gates. The range of \bar{m} is such that the condition after Eq. (19) is met for our chosen values of the unknown coupling g , so that the QFI is well approximated by its leading order term. The vertical and horizontal dotted lines locate the saturation point (23) where the energy plateau starts. This matches the behaviour indicated by the dashed curve in Figure 1(c). Solid and dotted lines in the inset are the corresponding true and raw complexities (21), respectively. As already observed in Figure 2(b) and predicted in Appendix A, the latter approximates the former better as the error increases. (b) The total energy plot in (a) is repeated for various δ^2 and fixed $g = 2.5$. The blue solid curve depicts the evolution of the saturation point as both \bar{m} and δ^2 vary.

Note that here $E(\epsilon)$ diverges in the ideal limit of a perfect unitary implementation ($\epsilon \rightarrow 0$ or $\bar{m} \rightarrow \infty$) and so the total energy cost $R(\epsilon)$ is expected to decrease initially, matching the qualitative pattern illustrated in Figure 1. This is consistent with the battery model introduced in Section IV A, which predicates a diverging implementation energy regardless of the physical model adopted, as long as the desired unitary phase-encoding channel U_g is not energy-conserving with respect to the qubit and the implementation energy equals the total energy of the coupled control operation [57, 64].

We plot R in Figure 4 within the approximation range. Starting from the ideal limit $1/\bar{m} \rightarrow 0$, the total energy cost goes through a sharp drop, then plateaus after a saturation point. Since the complexity increases with $1/\bar{m}$, this point may serve as the *sweet spot* for complexity-energy co-optimisation, beyond which energy saving becomes inefficient with respect to complexity overhead. Reading from the graph, the plateau appears around when more than one repetition of the sequence takes place and the sweet spot can be located by setting $q_{N_{\text{opt}}} = 1$ in Eq. (20) and using Eqs. (21), (22), which leads to

$$\bar{m}_0 \approx \Delta(g) \sqrt{\frac{e}{\delta^2}}, \quad C_0 \approx \sqrt{\frac{e}{\delta^2}}, \quad R_0 \approx \frac{e\Delta(g)}{\delta^2}. \quad (23)$$

From Eq. (21), the product $c \cdot \bar{m} \approx R_0$ does not depend on \bar{m} , explaining the flattening up to the leading order.

Two remarks are in order. First, the implementation error of the phase-encoding channel, as modelled in this Section, comes solely from the quantum fluctuation of the EM field. In

particular, we treat the field parameters as random variables instead of quantum operators and only extract the leading order effect to allow an analytical derivation. In doing so we have ignored other sources of noise, including laser inefficiency, decoherence caused by system-environment interaction, and higher-order effects from the field fluctuation which become significant if the field power is reduced.

Second, a caveat in identifying the sweet spot concerns the attainability of the quantum Cramér–Rao bound (6). Recall that the bound is tight only in the asymptotic limit, requiring in principle many repetitions, whereas the energy-optimal regime identified here involves only a small number of repetitions. Our analysis therefore uses the QFI metric as a benchmark rather than a guarantee of achievable performance. Finite-sample effects may shift the precise location of the optimum, but do not alter the qualitative trade-off between implementation quality and repetition cost. As shown in Appendix D, operating at a smaller photon number per gate \bar{m} , in particular in the regime $10^2 \lesssim \bar{m} \lesssim 5 \cdot 10^2$, improves the consistency between the actual estimator performance and the asymptotic bound.

C. Other Sources of Cost

1. Complexity and Energy Minimisation

Apart from gate implementation, other components of the protocol also cost energy to implement and they may have impact on the complexity as well. We will next consider a few of these contributions for a more complete energy bookkeeping (see also Appendix C), namely the tasks of state preparation and measurement at the beginning and end of each sequence, respectively. Before proceeding, we first describe qualitatively the difference brought by the additional cost.

The two key quantities involved in the trade-off relation as illustrated in Figure 1 are the complexity C , or the minimal number of gates needed to reach a set objective (10), and the corresponding total energy cost R . For the latter, we now take into account the additional (or ‘external’) cost of each sequence other than the one spent on gate implementation, denoted as E_{ext} . Here it is treated as a constant for simplicity, while in general it may depend on parameters that can also affect the complexity, as we will see in Section IV C 2. The total energy cost as a function of the sequence steps number N is accordingly modified as

$$R_N \equiv R_N(\bar{m}; g, \delta^2, E_{\text{ext}}) = \begin{cases} \underbrace{(NQ_N + N_0)}_{\text{number of gates}} \times \bar{m} + \underbrace{(Q_N + 1)}_{\text{number of sequences}} \times E_{\text{ext}} & \text{if } N_0 > 0; \\ NQ_N \times \bar{m} + Q_N \times E_{\text{ext}} & \text{if } N_0 = 0. \end{cases} \quad (24)$$

We may denote N_C and N_R as the steps that minimise the total number of gates and the total energy cost, respectively, with the same constraint as in Eq. (10):

$$\begin{aligned} N_C &\equiv N_C(\bar{m}; g, \delta^2) = \arg \min_N (NQ_N + N_0) \Big|_{\delta^2}, \\ N_R &\equiv N_R(\bar{m}; g, \delta^2, E_{\text{ext}}) = \arg \min_N (R_N) \Big|_{\delta^2}. \end{aligned} \quad (25)$$

In Section IV B, $E_{\text{ext}} = 0$ and the two optimal steps coincide, $N_C = N_R$. However, with the additional energy cost they start to differ and the step optimisation becomes dependent on the quantity to be minimised. By construction, optimising for the total number of gates will result in a lower complexity at the expense of a higher total energy cost,

$$R_{N_C} \geq R_{N_R}, \quad (26)$$

and vice versa, with the equality attained if $E_{\text{ext}} = 0$.

2. State Preparation

State preparation often aims to cool a thermal state from its initial temperature to a lower one. In our case, the ideal initial state of the system qubit is $|0\rangle\langle 0|$. However, the third law

of thermodynamics implies that any process cannot reach zero temperature, corresponding to a pure state, with finite resource [70], and so the cooled state can only lie in the vicinity of $|0\rangle\langle 0|$. For the implementation, we adopt the technique of dynamic cooling [71, 72]. Consider M_s identical qubits, with one target system and $M_s - 1$ auxiliary qubits. They are governed by the same Hamiltonian, $H_i = -\hbar\omega_0\sigma_z^{(i)}/2$, $i = 1, 2, \dots, M_s$. Their initial state is a product of thermal states with environmental temperature T_0 :

$$\rho_\beta = \bigotimes_{i=1}^{M_s} \left(\frac{e^{-\beta H_i}}{Z(\beta)} \right), \quad (27)$$

where $\beta = 1/k_B T_0$, k_B being Boltzmann’s constant, and $Z(\beta)$ is the corresponding partition function. A unitary operation V_{sp} then acts on all qubits and the auxiliary ones are discarded afterwards, leaving the system qubit in a state with new temperature $T < T_0$. It is shown [72] that in the low temperature regime, the minimal temperature the cooling can reach is

$$T \approx \frac{2T_0}{M_s}, \quad \text{if } k_B T_0 \ll \hbar\omega_0. \quad (28)$$

The energy cost of state preparation is again interpreted as in Section IV A. Here the initial state ρ_β is considered free of cost [73, 74], as it is in thermal equilibrium with the environment. The cost W comes from the energy change of the qubits induced by the non-energy-conserving unitary V_{sp} , and the ensuing free operation consists of discarding the auxiliary qubits. Eq. (15) thus reads

$$W = \text{Tr} \left[\left(\sum_i H_i \right) (V_{sp} \rho_\beta V_{sp}^\dagger - \rho_\beta) \right]. \quad (29)$$

According to the model of Figure 3, W can be interpreted as the free energy drawn from an external battery [75] to implement the cooling unitary.

Ref. [72] shows that W in Eq. (29) is an extensive quantity and the energy cost per qubit in the thermodynamic limit is

$$\bar{w} = \lim_{M_s \rightarrow \infty} \frac{W}{M_s} = \frac{\omega_0}{2\omega} \frac{\tanh\left(\frac{1}{2\xi}\right)}{e^{\frac{1}{\xi}} + 1}, \quad \xi = \frac{k_B T_0}{\hbar\omega_0}, \quad (30)$$

where the energy unit remains the photonic energy of the EM field. As seen shortly, in practice only a small number of cooling qubits are needed for energy optimisation and so the thermodynamic limit does not apply. For small T_0 we can nevertheless approximate \bar{w} as the energy change of each qubit. The external cost per round for state preparation is then

$$E_{\text{ext}}^{(\text{preparation})} = \bar{w} \cdot M_s. \quad (31)$$

This quantity later turns out to be much smaller than the cost of gate implementation for state-of-the-art technology. In this subsection we will thus ignore the distinction between complexity and energy minimisation introduced in Section IV C 1.

After cooling, each sequence now starts with the initial state

$$\rho_0(T) = \frac{e^{-\beta H_i}}{Z(\beta)} = \frac{1 + \gamma(T)}{2} |0\rangle\langle 0| + \frac{1 - \gamma(T)}{2} |1\rangle\langle 1|, \quad (32)$$

where $\gamma(T) = \tanh\left(\frac{\hbar\omega_0}{2k_B T}\right)$ characterises the closeness to $|0\rangle\langle 0|$ as the Bloch vector of ρ_0 is $[0, 0, \gamma(T)]^\top$. Derivations in

Appendix B imply that the leading correction to the QFI due to the non-ideal initial state is a multiplicative factor of $[\gamma(T)]^2$. With Eq. (28) this yields modification on Eqs. (19)–(21) as

$$\begin{aligned} F_N(\bar{m}; g) &\xrightarrow{\text{state preparation}} F_N(\bar{m}; g, M_s) \approx \left[\gamma\left(\frac{2T_0}{M_s}\right)\right]^2 \cdot F_N(\bar{m}; g); \\ N_{\text{opt}}(\bar{m}; g) &\xrightarrow{\text{state preparation}} N_{\text{opt}}(\bar{m}; g, M_s) \approx N_{\text{opt}}(\bar{m}; g); \\ q_{N_{\text{opt}}}(\bar{m}; g, \delta^2) &\xrightarrow{\text{state preparation}} q_{N_{\text{opt}}}(\bar{m}; g, \delta^2, M_s) \approx \left[\gamma\left(\frac{2T_0}{M_s}\right)\right]^{-2} q_{N_{\text{opt}}}(\bar{m}; g, \delta^2); \\ c(\bar{m}; g, \delta^2) &\xrightarrow{\text{state preparation}} c(\bar{m}; g, \delta^2, M_s) \approx \left[\gamma\left(\frac{2T_0}{M_s}\right)\right]^{-2} c(\bar{m}; g, \delta^2). \end{aligned} \quad (33)$$

The total energy cost is computed through Eq. (24), with N determined by the minimisation in (10) and E_{ext} given by Eq. (31). For small \bar{m} , this can be approximated through the raw complexity: using Eq. (33) on Eq. (24) leads to,

$$R(\bar{m}; g, \delta^2, M_s) \approx \frac{e}{\delta^2} \cdot \frac{\Delta(g)^2}{\bar{m}^2} \cdot \frac{\bar{w}M_s + \frac{\bar{m}^2}{\Delta(g)}}{\left[\tanh\left(\frac{M_s}{4\xi}\right)\right]^2}. \quad (34)$$

A characteristic value of ξ for contemporary quantum technologies based on techniques such as superconducting and ion trap qubits is approximately 0.2 [76, 77]; Eq. (30) then yields $\bar{w} \approx 0.003$, where we take advantage of the resonance condition $\omega \approx \omega_0$. Within this range, Figure 5 shows that the total energy cost quickly converges to a minimal value when more cooling qubits are consumed per sequence. From Eq. (34) we anticipate the total cost to eventually increase with M_s — complexity reduction brought by further cooling is overpowered by its energy cost. However, this does not manifest until M_s grows significantly large, since the relative magnitude between the cost of state preparation and gate implementation is as small as

$$\frac{\text{cost of states}}{\text{cost of gates}} \sim \frac{\bar{w}M_s\Delta(g)}{\bar{m}^2} \sim 10^{-7}M_s. \quad (35)$$

3. Measurement

To implement the measurement procedure we adopt the pointer model [78, 79]: the system qubit is coupled to a pointer qubit through a CNOT gate controlled by the system, the pointer is measured with respect to the optimal POVM and the outcome should follow the statistics of the system state. The pointer thus acts as a measuring device. Let it be governed by the Hamiltonian $-\hbar\omega_1\sigma_z/2$, ω_1 being the transition frequency.

For perfect measurement, we want to initialise the pointer in $|0\rangle\langle 0|$. However, again, a pure state requires an infinite amount of resource to prepare, and so does an ideal projective measurement [80]. The resulting non-ideal measurement affects the QPE performance [81, 82]. In Appendix E we evaluate the

CFI from a mixed pointer state prepared through the dynamic cooling protocol. Despite the imperfection, as observed in Section IV C 2, in current setups the energy cost of cooling is negligible compared to that of the phase-encoding gate implementation for energy optimisation. We will therefore assume the initial pointer state is $|0\rangle\langle 0|$ for free. For an N -step sequence the system-pointer state prior to the correlating gate is then of the form $\rho_N^{(S)} \otimes |0\rangle\langle 0|^{(P)}$, where superscripts are used to label the two parts. This is taken as the free initial state in the bookkeeping model of Figure 3 when formalising the energy cost, while measurement on the pointer and discarding of the system qubit amount to the free operations at the end. The cost in this case comes from the correlating CNOT gate: the resulting energy increase it causes on the pointer qubit (since the system qubit acts as the control, its energy is not changed) is given by

$$\begin{aligned} E_{\text{ext}}^{(\text{measurement})} &= \text{Tr} \left[\left(\mathcal{I}^{(S)} \otimes \frac{-\omega_1}{2\omega} \sigma_z^{(P)} \right) \cdot \right. \\ &\quad \left. \left(\text{CNOT}(\rho_N^{(S)} \otimes |0\rangle\langle 0|^{(P)}) \text{CNOT}^\dagger - \rho_N^{(S)} \otimes |0\rangle\langle 0|^{(P)} \right) \right] \\ &= \langle 1 | \rho_N^{(S)} | 1 \rangle \cdot \frac{\omega_1}{\omega}, \end{aligned} \quad (36)$$

in units of the photonic energy. Here $E_{\text{ext}}^{(\text{measurement})}$ depends on the system state just before the CNOT gate is applied. For both simplicity and generality, we will instead use the loose yet constant upper bound on the correlating cost, namely the gap between the two energy levels of the pointer qubit:

$$E_{\text{ext}}^{(\text{measurement})} \cong \frac{\omega_1}{\omega}. \quad (37)$$

Both types of total energy cost in Eq. (26) are plotted in Figure 6 for a range of $\frac{\omega_1}{\omega}$ chosen for illustrative purpose. Note that they are within the approximation range according to Eq. (35) — replacing ω_0 with ω_1 when computing \bar{w} in Eq. (30) — to validate the omission of the state preparation (cooling) cost for the pointer.

The gap between the two costs emphasises the importance of deciding the optimisation priority between complexity and energy, a task closely related to practical constraints. Finally, recall Eq. (23) and its preceding arguments. Due to the additional cost each round, the sweet spot now becomes a turning

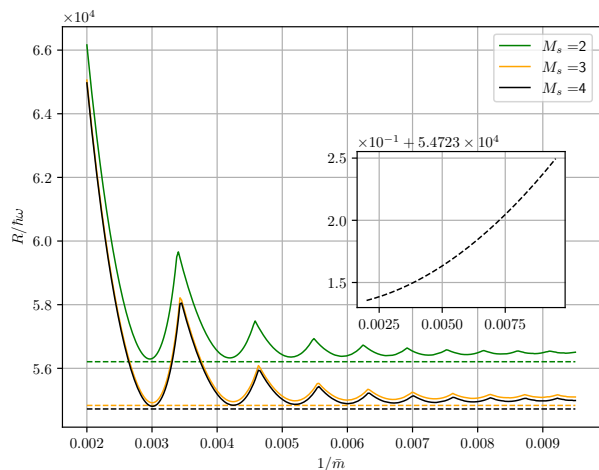


FIG. 5. Plots of the total energy cost (in units of $\hbar\omega$) of implementing the phase-encoding gate (see Figure 4), now combined with that of state preparation for initialising the probe qubit, with $g = 2.5$, $\xi = 0.2$, $\delta^2 = 10^{-4}$ and the error represented by $1/\bar{m}$. The number of cooling qubits used per sequence, M_s , is also varied to show that small amount of cooling suffices to approach the ideal limit. Solid lines are computed by Eq. (24), while dashed ones (34) approximate the cost through the raw complexity. Contrary to the plateau in Figure 4, the total energy cost ends up increasing with larger implementation error as shown in the inset, since a larger error, or smaller \bar{m} , leads to more repetitions (see Eq. (20)) and hence a larger cooling cost. This corresponds to the behaviour indicated by the solid curve in Figure 1(c). However, the increment is negligible and only observable by the zoom-in in the inset as the cost of cooling is much smaller than that of gate implementation.

point of the total energy cost as a function of the implementation error. This characteristic — reminiscent of the qualitative behaviour displayed by the solid curve in Figure 1(c) — further justifies the spot as a feasible candidate for complexity-energy co-optimisation. Interestingly, such an optimal working point is uniquely identified regardless of which minimisation is chosen for the number of steps, as the gap between R_{N_C} and R_{N_R} only begins to open up at larger error values.

D. Discussion

Figure 7 summarises the QPE protocol constructed in this Section. For a fixed number of photons \bar{m} spent on each gate, we have determined the minimal number of gates needed, or the complexity, and their spatial arrangement to reach a desired lower bound on the estimator variance. We have also analysed the corresponding total energy cost and identifying a sweet spot for complexity-energy co-optimisation while varying \bar{m} .

As mentioned at the end of Section II, our energy analysis on the QPE protocol fits naturally into the MNR framework [33, 34]. In Eq. (4), we can identify the *metric* as the total QFI of the sequential protocol, constrained by the target bound $1/\delta^2$, while the *resource* is the total energy cost R computed so far. The *noise* in our case comes from the quantum fluctuation

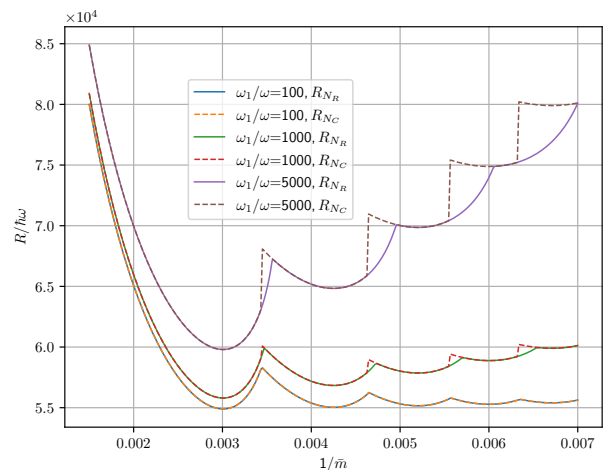


FIG. 6. Plots of the combined total energy cost of measurement and gate implementation (in units of $\hbar\omega$). The fixed parameters are $g = 2.5$, $\delta^2 = 10^{-4}$. Solid and dashed lines correspond to when the total energy cost and the number of gates are minimised, respectively amounting to R_{N_R} and R_{N_C} ; see Eqs. (24)–(26), with the measurement cost E_{ext} given by Eq. (37), or ω_1/ω . The two costs coincide when they involve the same number of complete sequences, Q_N , since then their measurement costs, $E_{\text{ext}} \cdot (Q_N + 1)$, are the same and so minimising the total energy cost and only the cost of gate implementation are equivalent. Otherwise, a gap opens up between R_{N_C} and R_{N_R} when the numbers of full sequences for each differ. This happens when the measurement cost of an extra sequence outweighs the cost of the gates it saves for complexity minimisation. Observe that, the larger and the smaller E_{ext} and \bar{m} are, respectively, the larger the gap grows between the two energy costs and the choice regarding which quantity to optimise becomes more important.

of the EM field. Therefore, for each fixed δ^2 , maximising the efficiency (4), $\eta = \frac{1}{\delta^2 R}$, is equivalent to minimising the total energy cost.

When only the cost of the sequential gate implementation is factored in as in Section IV B, the minimal cost corresponds to the saturation point (23). In this case the efficiency becomes independent of the metric: $\eta = \frac{1}{\delta^2 R_0} = \frac{1}{e\Delta(g)}$. Once the other sources of cost — including but not limited to the ones analysed in Section IV C — kick in, the total energy cost increases and the metric dependence of the efficiency starts to show. Therefore, within the MNR framework the QPE protocol constructed in this Section has an efficiency upper bounded by

$$\eta \leq \frac{1}{e\Delta(g)}. \quad (38)$$

From Eq. (19), $\Delta(g)$ is a monotonically increasing function of g and so, the larger the unknown parameter g , the less energy-efficient the QPE protocol is.

The energy plateau observed in Fig. 4 motivates us to ask if the asymptotic scaling of the total energy cost with the implementation error can be inferred from just a small set of parameters that are well-defined for all physical realisations of

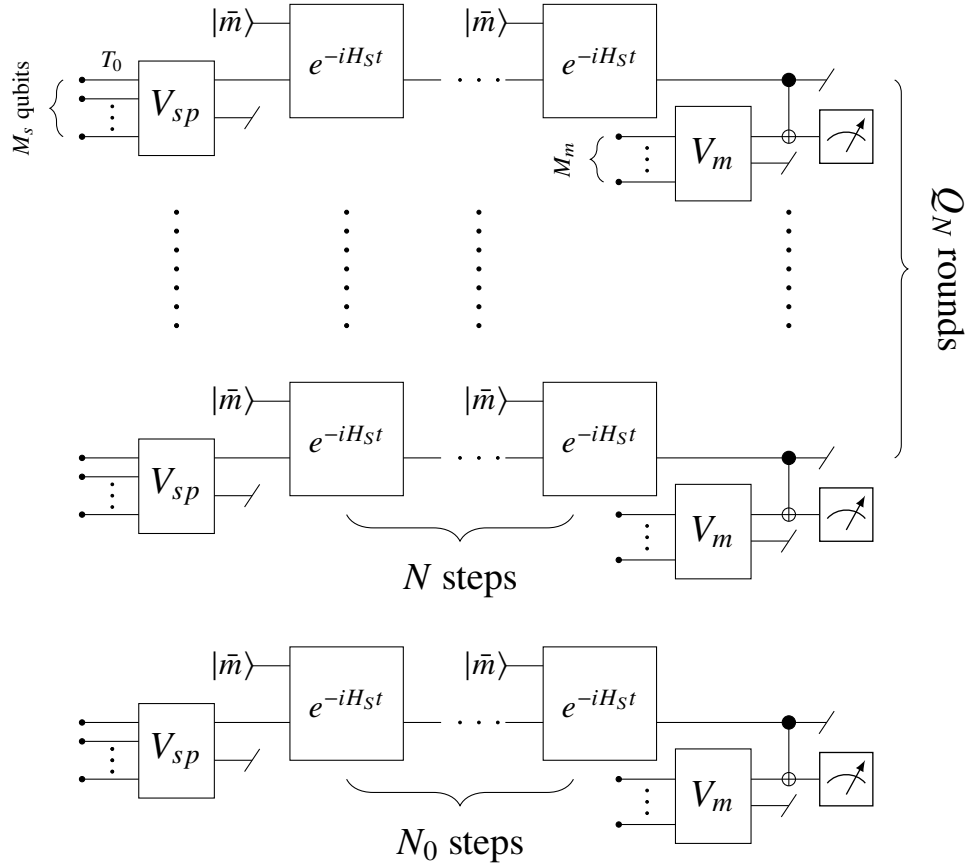


FIG. 7. Full circuit diagram of the QPE protocol for which a trade-off between complexity and energy is established in this work.

the QPE protocol, so that qualitative conclusions can be drawn in a universal fashion. This can serve for both theoretical and engineering purposes in designing energy-optimal physical realisations of sequential QPE tasks. Here we undertake a preliminary investigation and determine a condition for the energy plateau to exist.

First, we state our general assumptions, which hold in particular for the optical implementation analysed in this Section:

- We will stay in the semi-classical regime so that the implementation error ϵ can be treated as a small parameter;
- Meanwhile, ϵ shall also be large enough such that the raw complexity well approximates the true complexity;
- Recalling the qualitative form of the QFI in Eq. (A1),

$$F_N = N^2 e^{-f(N, \epsilon)},$$

the exponent f will be assumed to grow no more than polynomially as a function of the number of steps N ;

- The implementation energy of each phase-encoding gate will be assumed to follow an inverse power law [58], so that $E(\epsilon) \sim \epsilon^{-\tau}$ for some $\tau > 0$.

In the ideal limit of vanishing implementation error, $\epsilon = 0$, we reach the Heisenberg limit of a sequential QPE strategy [83], $F_N \propto N^2$. Without loss of generality, set $f(N, 0) = 0$

so that the constant of proportionality is 1. Then, f admits a power series expansion with respect to $\epsilon \rightarrow 0$ with some leading order $\nu > 0$:

$$f(N, \epsilon) \approx g(N)\epsilon^\nu,$$

for some polynomially-bounded function $g(N)$. The optimal step N_{opt} for the raw complexity (8) is determined by minimising the quantity $Nf(N, \epsilon)$, leading to

$$N_{\text{opt}} \frac{\partial f(N_{\text{opt}}, \epsilon)}{\partial N} = 1 \quad \longrightarrow \quad N_{\text{opt}} g'(N_{\text{opt}}) \approx \epsilon^{-\nu}.$$

Let $g(N)$ admit a power series expansion with leading order $q > 0$, so that $g(N) \approx c_q N^q$ as $N \rightarrow \infty$. The optimal step and the corresponding raw complexity can then be expressed as

$$N_{\text{opt}} \approx (c_q q \epsilon^\nu)^{-1/q},$$

$$c(\epsilon; \delta^2) = \frac{1}{\delta^2 N_{\text{opt}} e^{-f(N_{\text{opt}}, \epsilon)}} \approx \delta^{-2} e^{1/(c_q q)} (c_q q \epsilon^\nu)^{1/q}.$$

Within the regime of validity of our assumptions, the total energy cost (3) then behaves as

$$R(\epsilon; \delta^2) = E(\epsilon) \times c(\epsilon; \delta^2) \sim \mathcal{O}(\epsilon^{\frac{\nu}{q} - \tau}). \quad (39)$$

Observe that $\nu = q\tau$ and $\nu > q\tau$ correspond to the dashed and solid curve in Figure 1, respectively, where the total energy

cost either eventually plateaus or exhibits a global minimum; on the other hand, $\nu < q\tau$ indicates that the total energy cost vanishes asymptotically, which is incompatible with the stated assumptions.

The example in Section IV B has $\epsilon = 1/\bar{m}$, and so, according to Eq. (19), $f(N, \epsilon) = -2N \log(1 - \Delta(g)\epsilon/2)$ with $\nu = 1$, $q = 1$ and $c_q = \Delta(g)$. The energy cost per gate is proportional to the photon number, $\tau = 1$. Thus $q\tau = 1 = \nu$ yields the energy plateau as expected. Including the additional costs associated with state preparation and measurement effectively reduces τ : this breaks the plateau and pushes the total energy (39) in the regime $\nu > q\tau$, leading to the appearance of the turning point as identified in Section IV C.

V. CONCLUDING REMARKS AND OUTLOOK

In this work, we have established a framework for analysing and quantifying the trade-off between gate complexity and energy cost in quantum processes composed of elementary building blocks. We have applied our framework to the case study of a sequential quantum phase estimation protocol and identified physical conditions for the joint optimisation of complexity and energy, given a target metric benchmarking the desired estimation precision. Our analysis rests on a consistent characterisation of energy cost in different components of the protocol, encompassing input probe state preparation, phase-encoding gate implementation, and output measurement.

As mentioned in the Introduction, all components other than the phase-encoding channel (11) compose of an estimation strategy for the metrology task. A strategy that obeys causal order can be represented by a quantum comb [84–88]. Combs introduce more general structures to the current protocol, most notably temporal and spatial correlation such as entanglement amongst the probe qubits of each sequence (improvement brought by entangled probes to the model in Section III C has been studied by Ref. [89]), memory effects throughout the implemented gates carried by ancilla, and correlated decoherence noise [90]. Furthermore, causally indefinite strategies, such as a quantum switch [91], have the potential to surpass the Heisenberg limit [92–94]. Meanwhile, the energy cost of quantum combs for metrology has been studied less, with Ref. [39] being one recent development (see also Ref. [95] for a complementary study on work extraction from quantum combs). Combining the above results and the one in this work can help determine the trade-off relation between complexity and total energy cost of both components — estimation strategy and parameter-encoding process —

of a quantum metrology task, leading to a more complete complexity-energy co-optimisation.

It is also worth remarking that quantum resource can come in different forms other than energy. For the QPE protocol, Ref. [96] studies how the quality of the estimate can be quantified by quantum coherence, while Ref. [83] explains how entanglement amongst the probes leads to the quantum speed-up. Therefore, a more general framework should be able to account for different types of resource cost in a consistent fashion. This may be achieved by constructing proper conversion schemes between these resources [97], which, for example, may help determine the energy cost of generating entanglement [98–100] and coherence [101, 102], or by designing case-dependent hybrid cost functions.

Finally, the building principle of this work may be adopted in other quantum tasks with structures similar to (1): as long as the quantum protocol is composed of some elementary units, then generally, the less energy spent on each unit, the larger the implementation error will be, leading to greater unit complexity. In Section IV D we obtain a qualitative understanding on how the trade-off framework applies to a QPE protocol without referring to the specific physical model at hand. To make a clear analogy with other quantum protocols, the essential ingredient is a metric $\mathcal{M}(N, \epsilon)$ that depends on the number of units N and their implementation error ϵ , and can be used to assess the performance of a quantum protocol quantitatively. For the examples mentioned in Section I, such a metric can be the QFI used in this work (in the context of quantum metrology), the overlap between the final state and the target state searched for (in Grover’s algorithm), the norm distance between the overall implemented gate and the desired Hamiltonian evolution (in Hamiltonian simulation), etc. Therefore, the lines of reasoning presented in this paper can be straightforwardly adapted to many other common applications. A comprehensive analysis on practical complexity-energy trade-off relations for existing and upcoming quantum technology primitives will be pivotal for their sustainable development and widespread impact.

ACKNOWLEDGMENTS

This work was supported by the Engineering and Physical Sciences Research Council (EPSRC Grants No. EP/W524402/1, EP/T022140/1, and EP/X010929/1). We acknowledge fruitful discussions with Longyun Chen, Yuxiang Yang, Florian Meier, Victor Montenegro, Hiroyasu Tajima, Francesco Albarelli, Salvatore Tirone and Tommaso Tufarelli.

* yukuan.tao@nottingham.ac.uk

† madalin.guta@nottingham.ac.uk

‡ gerardo.adesso@nottingham.ac.uk

[1] A. Streltsov, G. Adesso, and M. B. Plenio, Colloquium: Quan-

tum coherence as a resource, *Rev. Mod. Phys.* **89**, 041003 (2017).

[2] C. Eltschka and J. Siewert, Quantifying entanglement resources, *Journal of Physics A: Mathematical and Theoretical*

- 47, 424005 (2014).
- [3] E. Chitambar and M.-H. Hsieh, Relating the resource theories of entanglement and quantum coherence, *Physical Review Letters* **117**, 2 (2016).
 - [4] E. Chitambar and G. Gour, Quantum resource theories, *Reviews of Modern Physics* **91**, 2 (2019).
 - [5] M. A. Nielsen and I. L. Chuang, *Quantum Computation and Quantum Information: 10th Anniversary Edition* (Cambridge University Press, 2010).
 - [6] A. W. Harrow and A. Montanaro, Quantum computational supremacy, *Nature* **549**, 203 (2017).
 - [7] L. K. Grover, A fast quantum mechanical algorithm for database search, in *Proceedings of the twenty-eighth annual ACM symposium on Theory of computing* (1996) pp. 212–219.
 - [8] P. W. Shor, Polynomial-time algorithms for prime factorization and discrete logarithms on a quantum computer, *SIAM Journal on Computing* **26**, 1484–1509 (1997).
 - [9] V. Mavroeidis, K. Vishi, M. D., and A. Jøssang, The impact of quantum computing on present cryptography, *International Journal of Advanced Computer Science and Applications* **9**, 3 (2018).
 - [10] S. Lloyd, Universal quantum simulators, *Science* **273**, 1073 (1996).
 - [11] G. H. Low and I. L. Chuang, Hamiltonian simulation by qubitization, *Quantum* **3**, 163 (2019).
 - [12] R. Feynman, Simulating physics with computers., *International Journal of Theoretical Physics* **21**, 467 (1982).
 - [13] V. Giovannetti, S. Lloyd, and L. Maccone, Quantum-enhanced measurements: Beating the standard quantum limit, *Science* **306**, 1330–1336 (2004).
 - [14] V. Giovannetti, S. Lloyd, and L. Maccone, Quantum metrology, *Phys. Rev. Lett.* **96**, 010401 (2006).
 - [15] V. Giovannetti, S. Lloyd, and L. Maccone, Advances in quantum metrology, *Nature Photonics* **5**, 222–229 (2011).
 - [16] K. Bongs, R. Launay, and M. A. Kasevich, High-order inertial phase shifts for time-domain atom interferometers, *Applied Physics B* **84**, 599 (2006).
 - [17] M. A. Taylor, J. Janousek, V. Daria, J. Knittel, B. Hage, H.-A. Bachor, and W. P. Bowen, Biological measurement beyond the quantum limit, *Nature Photonics* **7**, 229–233 (2013).
 - [18] H. Katori, Optical lattice clocks and quantum metrology, *Nature Photonics* **5**, 203 (2011).
 - [19] W. H. Zurek, Decoherence, einselection, and the quantum origins of the classical, *Rev. Mod. Phys.* **75**, 715 (2003).
 - [20] P. J. Salas, Noise effect on grover algorithm, *The European Physical Journal D* **46**, 365–373 (2007).
 - [21] D. Shapira, S. Mozes, and O. Biham, Effect of unitary noise on grover’s quantum search algorithm, *Phys. Rev. A* **67**, 042301 (2003).
 - [22] N. Shenvi, K. R. Brown, and K. B. Whaley, Effects of a random noisy oracle on search algorithm complexity, *Phys. Rev. A* **68**, 052313 (2003).
 - [23] I. L. Chuang, R. Laflamme, P. W. Shor, and W. H. Zurek, Quantum computers, factoring, and decoherence, *Science* **270**, 1633–1635 (1995).
 - [24] R. Demkowicz-Dobrzański, J. Kołodyński, and M. Guła, The elusive Heisenberg limit in quantum-enhanced metrology, *Nature Communications* **3**, 1 (2012).
 - [25] J. Kołodyński and R. Demkowicz-Dobrzański, Phase estimation without a priori phase knowledge in the presence of loss, *Phys. Rev. A* **82**, 053804 (2010).
 - [26] P. Sekatski, M. Skotiniotis, J. Kołodyński, and W. Dür, Quantum metrology with full and fast quantum control, *Quantum* **1**, 27 (2017).
 - [27] D. A. Lidar and T. A. Brun, *Quantum Error Correction* (Cambridge University Press, 2013).
 - [28] S. Zhou, M. Zhang, J. Preskill, and L. Jiang, Achieving the heisenberg limit in quantum metrology using quantum error correction, *Nature Communications* **9**, 1 (2018).
 - [29] R. Demkowicz-Dobrzański, J. Czajkowski, and P. Sekatski, Adaptive quantum metrology under general markovian noise, *Phys. Rev. X* **7**, 041009 (2017).
 - [30] E. Campbell, A series of fast-paced advances in quantum error correction, *Nature Reviews Physics* **6** (2024).
 - [31] R. Acharya *et al.*, Quantum error correction below the surface code threshold, *Nature* **638**, 920–926 (2024).
 - [32] J. Preskill, Quantum computing in the nisq era and beyond, *Quantum* **2**, 79 (2018).
 - [33] A. Auffèves, Quantum technologies need a quantum energy initiative, *PRX Quantum* **3**, 020101 (2022).
 - [34] M. Fellous-Asiani, J. H. Chai, Y. Thonnart, H. K. Ng, R. S. Whitney, and A. Auffèves, Optimizing resource efficiencies for scalable full-stack quantum computers, *PRX Quantum* **4**, 040319 (2023).
 - [35] M. Fellous-Asiani, J. H. Chai, R. S. Whitney, A. Auffèves, and H. K. Ng, Limitations in quantum computing from resource constraints, *PRX Quantum* **2**, 040335 (2021).
 - [36] P. Lipka-Bartosik and R. Demkowicz-Dobrzański, Thermodynamic work cost of quantum estimation protocols, *Journal of Physics A: Mathematical and Theoretical* **51**, 474001 (2018).
 - [37] P. Liuzzo-Scorpo, L. A. Correa, F. A. Pollock, A. Górecka, K. Modi, and G. Adesso, Energy-efficient quantum frequency estimation, *New Journal of Physics* **20**, 063009 (2018).
 - [38] V. Montenegro, S. Dornetti, A. Ferraro, and M. G. A. Paris, Enhanced quantum frequency estimation by nonlinear scrambling, *Phys. Rev. Lett.* **135**, 030802 (2025).
 - [39] L. Chen and Y. Yang, Optimal quantum metrology under energy constraints (2026).
 - [40] F. Meier and H. Yamasaki, Energy-consumption advantage of quantum computation, *PRX Energy* **4**, 023008 (2025).
 - [41] D. Jaschke and S. Montangero, Is quantum computing green? an estimate for an energy-efficiency quantum advantage, *Quantum Science and Technology* **8**, 025001 (2023).
 - [42] J. Thompson, P. M. Riechers, A. J. P. Garner, T. J. Elliott, and M. Gu, Energetic advantages for quantum agents in online execution of complex strategies, *Phys. Rev. Lett.* **135**, 160402 (2025).
 - [43] S. L. Braunstein and C. M. Caves, Statistical distance and the geometry of quantum states, *Phys. Rev. Lett.* **72**, 3439 (1994).
 - [44] G. Tóth and I. Apellaniz, Quantum metrology from a quantum information science perspective, *Journal of Physics A: Mathematical and Theoretical* **47**, 424006 (2014).
 - [45] A. S. Holevo, *Probabilistic and statistical aspects of quantum theory*, Vol. 1 (Springer Science & Business Media, 2011).
 - [46] M. G. Paris, Quantum estimation for quantum technology, *International Journal of Quantum Information* **7**, 125 (2009).
 - [47] B. L. Higgins, D. W. Berry, S. D. Bartlett, H. M. Wiseman, and G. J. Pryde, Entanglement-free heisenberg-limited phase estimation, *Nature* **450**, 393–396 (2007).
 - [48] R. Nichols, T. R. Bromley, L. A. Correa, and G. Adesso, Practical quantum metrology in noisy environments, *Phys. Rev. A* **94**, 042101 (2016).
 - [49] R. Demkowicz-Dobrzański and L. Maccone, Using entanglement against noise in quantum metrology, *Phys. Rev. Lett.* **113**, 250801 (2014).
 - [50] U. Dorner, R. Demkowicz-Dobrzanski, B. J. Smith, J. S. Lundeen, W. Wasilewski, K. Banaszek, and I. A. Walmsley, Optimal quantum phase estimation, *Phys. Rev. Lett.* **102**, 040403

- (2009).
- [51] R. A. Fisher, Dispersion on a sphere, in *Proceedings of the Royal Society of London. Series A. Mathematical and Physical Sciences*, Vol. 217 (1953) pp. 295 – 305.
- [52] A. Smirne, J. Kołodyński, S. F. Huelga, and R. Demkowicz-Dobrzański, Ultimate precision limits for noisy frequency estimation, *Phys. Rev. Lett.* **116**, 120801 (2016).
- [53] B. P. Abbott *et al.* (LIGO Scientific Collaboration and Virgo Collaboration), Observation of gravitational waves from a binary black hole merger, *Phys. Rev. Lett.* **116**, 061102 (2016).
- [54] R. Demkowicz-Dobrzański, K. Banaszek, and R. Schnabel, Fundamental quantum interferometry bound for the squeezed-light-enhanced gravitational wave detector geo 600, *Phys. Rev. A* **88**, 041802 (2013).
- [55] M. Pitkin, S. Reid, S. Rowan, and J. Hough, Gravitational wave detection by interferometry (ground and space), *Living Reviews in Relativity* **14**, 1 (2011).
- [56] R. Demkowicz-Dobrzański, M. Jarzyna, and J. Kołodyński, Quantum limits in optical interferometry, in *Progress in Optics* (Elsevier, 2015) p. 345–435.
- [57] G. Chiribella, Y. Yang, and R. Renner, Fundamental energy requirement of reversible quantum operations, *Phys. Rev. X* **11**, 021014 (2021).
- [58] J. Gea-Banacloche, Minimum energy requirements for quantum computation, *Phys. Rev. Lett.* **89**, 217901 (2002).
- [59] T. Karasawa, J. Gea-Banacloche, and M. Ozawa, Gate fidelity of arbitrary single-qubit gates constrained by conservation laws, *Journal of Physics A: Mathematical and Theoretical* **42**, 225303 (2009).
- [60] M. Ozawa, Conservative quantum computing, *Physical Review Letters* **89**, 5 (2002).
- [61] H. Tajima, N. Shiraishi, and K. Saito, Uncertainty relations in implementation of unitary operations, *Phys. Rev. Lett.* **121**, 110403 (2018).
- [62] H. Tajima, N. Shiraishi, and K. Saito, Coherence cost for violating conservation laws, *Phys. Rev. Res.* **2**, 043374 (2020).
- [63] H. Tajima, K. Yamaguchi, R. Takagi, and Y. Kuramochi, Universal tradeoff relations between resource cost and irreversibility of channels: General-resource wigner-araki-yanase theorems and beyond (2025), arXiv:2507.23760 [quant-ph].
- [64] In particular, Ref. [57] shows that, for any unitary V acting on the system space \mathcal{H}_S , we can find a battery state in the space \mathcal{H}_B with energy scaling $\sim 1/\sqrt{\varepsilon}$ and an energy-conserving unitary \tilde{V} on $\mathcal{H}_S \otimes \mathcal{H}_B$, such that the resulting quantum channel on the system alone approximates V with a worst-case fidelity at least $1 - \varepsilon$. Consequently, we can implement the desired unitary in each block with arbitrarily high fidelity by consuming a battery with sufficiently large stored energy. This does not incur extra cost, since the battery can be recycled for the next implementation and only the decrease in its energy contributes to the energy cost of the protocol.
- [65] E. K. Twyeffort Irish, J. Gea-Banacloche, I. Martin, and K. C. Schwab, Dynamics of a two-level system strongly coupled to a high-frequency quantum oscillator, *Phys. Rev. B* **72**, 195410 (2005).
- [66] J. Gea-Banacloche, Some implications of the quantum nature of laser fields for quantum computations, *Phys. Rev. A* **65**, 022308 (2002).
- [67] E. Jaynes and F. Cummings, Comparison of quantum and semiclassical radiation theories with application to the beam maser, *Proceedings of the IEEE* **51**, 89 (1963).
- [68] K. Igeta, N. Imoto, and M. Koashi, Fundamental limit to qubit control with coherent field, *Phys. Rev. A* **87**, 022321 (2013).
- [69] A. Silberfarb and I. H. Deutsch, Entanglement generated between a single atom and a laser pulse, *Phys. Rev. A* **69**, 042308 (2004).
- [70] L. Masanes and J. Oppenheim, A general derivation and quantification of the third law of thermodynamics, *Nature Communications* **8**, 1 (2017).
- [71] L. J. Schulman and U. V. Vazirani, Molecular scale heat engines and scalable quantum computation, in *Proceedings of the Thirty-First Annual ACM Symposium on Theory of Computing*, STOC '99 (Association for Computing Machinery, New York, NY, USA, 1999) p. 322–329.
- [72] L. Bassman Oftelie, A. De Pasquale, and M. Campisi, Dynamic cooling on contemporary quantum computers, *PRX Quantum* **5**, 3 (2024).
- [73] R. Gallego, J. Eisert, and H. Wilming, Thermodynamic work from operational principles, *New Journal of Physics* **18**, 103017 (2016).
- [74] M. Lostaglio, An introductory review of the resource theory approach to thermodynamics, *Reports on Progress in Physics* **82**, 114001 (2019).
- [75] F. Clivaz, R. Silva, G. Haack, J. B. Brask, N. Brunner, and M. Huber, Unifying paradigms of quantum refrigeration: Fundamental limits of cooling and associated work costs, *Phys. Rev. E* **100**, 042130 (2019).
- [76] A. Opremcak, C. H. Liu, C. Wilen, K. Okubo, B. G. Christensen, D. Sank, T. C. White, A. Vainsencher, M. Giustina, A. Megrant, B. Burkett, B. L. T. Plourde, and R. McDermott, High-fidelity measurement of a superconducting qubit using an on-chip microwave photon counter, *Phys. Rev. X* **11**, 011027 (2021).
- [77] T. P. Harty, D. T. C. Allcock, C. J. Ballance, L. Guidoni, H. A. Janacek, N. M. Linke, D. N. Stacey, and D. M. Lucas, High-fidelity preparation, gates, memory, and readout of a trapped-ion quantum bit, *Phys. Rev. Lett.* **113**, 220501 (2014).
- [78] J. von Neumann, R. Beyer, and N. Wheeler, *Mathematical Foundations of Quantum Mechanics: New Edition*, Princeton Landmarks in Mathematics and Physics (Princeton University Press, 2018).
- [79] C. Alexandre Brasil and L. Andreta de Castro, Understanding the pointer states, *European Journal of Physics* **36**, 065024 (2015).
- [80] Y. Guryanova, N. Friis, and M. Huber, Ideal Projective Measurements Have Infinite Resource Costs, *Quantum* **4**, 222 (2020).
- [81] Y. L. Len, T. Gefen, A. Retzker, and J. Kołodyński, Quantum metrology with imperfect measurements, *Nature Communications* **13**, 1 (2022).
- [82] S. Kurdziałek and R. Demkowicz-Dobrzański, Measurement noise susceptibility in quantum estimation, *Physical Review Letters* **130**, 16 (2023).
- [83] L. Maccone, Intuitive reason for the usefulness of entanglement in quantum metrology, *Phys. Rev. A* **88**, 042109 (2013).
- [84] P. Taranto, S. Milz, M. Muraio, M. T. Quintino, and K. Modi, Higher-order quantum operations (2025), arXiv:2503.09693 [quant-ph].
- [85] Q. Liu, Z. Hu, H. Yuan, and Y. Yang, Fully-optimized quantum metrology: Framework, tools, and applications, *Advanced Quantum Technologies* **7**, 12 (2024).
- [86] Q. Liu, Z. Hu, H. Yuan, and Y. Yang, Optimal strategies of quantum metrology with a strict hierarchy, *Phys. Rev. Lett.* **130**, 070803 (2023).
- [87] S. Kurdziałek, P. Dulian, J. Majsak, S. Chakraborty, and R. Demkowicz-Dobrzański, Quantum metrology using quantum combs and tensor network formalism, *New Journal of Physics* **27**, 013019 (2025).

- [88] G. Chiribella, G. M. D’Ariano, and P. Perinotti, Theoretical framework for quantum networks, *Phys. Rev. A* **80**, 022339 (2009).
- [89] R. Yousefjani, S. Salimi, and A. Khorashad, Enhancement of frequency estimation by spatially correlated environments, *Annals of Physics* **381**, 80–89 (2017).
- [90] S. Kurdziałek, F. Albarelli, and R. Demkowicz-Dobrzański, Universal bounds for quantum metrology in the presence of correlated noise, *Phys. Rev. Lett.* **135**, 130801 (2025).
- [91] G. Chiribella, G. M. D’Ariano, P. Perinotti, and B. Valiron, Quantum computations without definite causal structure, *Physical Review A* **88**, 022318 (2013).
- [92] X. Zhao, Y. Yang, and G. Chiribella, Quantum metrology with indefinite causal order, *Phys. Rev. Lett.* **124**, 190503 (2020).
- [93] L. Chen, Y.-X. Yang, G.-C. Li, X.-S. Hong, S.-Q. Zhang, H.-Q. Xu, Y.-C. Liu, G. Chiribella, G. Chen, C.-F. Li, and G.-C. Guo, Nonlinear enhancement of measurement precision via a hybrid quantum switch (2025), arXiv:2506.20632 [quant-ph].
- [94] P. Yin *et al.*, Experimental super-heisenberg quantum metrology with indefinite gate order, *Nature Physics* **19** (2023).
- [95] G. Zambon and G. Adesso, Quantum processes as thermodynamic resources: The role of non-markovianity, *Phys. Rev. Lett.* **134**, 200401 (2025).
- [96] F. Ahnefeld, T. Theurer, and M. B. Plenio, Coherence as a resource for phase estimation (2025), arXiv:2505.18544 [quant-ph].
- [97] A. Streltsov, U. Singh, H. S. Dhar, M. N. Bera, and G. Adesso, Measuring quantum coherence with entanglement, *Phys. Rev. Lett.* **115**, 020403 (2015).
- [98] L. Hackl and R. H. Jonsson, Minimal energy cost of entanglement extraction, *Quantum* **3**, 165 (2019).
- [99] C. Bény, C. T. Chubb, T. Farrelly, and T. J. Osborne, Energy cost of entanglement extraction in complex quantum systems, *Nature Communications* **9**, 1 (2018).
- [100] K. Horodecki, M. Winczewski, L. Sikorski, P. Mazurek, M. Czechlewski, and R. Yehia, Quantification of the energy consumption of entanglement distribution (2025), arXiv:2507.23108 [quant-ph].
- [101] A. Misra, U. Singh, S. Bhattacharya, and A. K. Pati, Energy cost of creating quantum coherence, *Physical Review A* **93**, 5 (2016).
- [102] I. Marvian, Operational interpretation of quantum fisher information in quantum thermodynamics, *Physical Review Letters* **129**, 19 (2022).
- [103] B. Escher, R. L. de Matos Filho, and L. Davidovich, General framework for estimating the ultimate precision limit in noisy quantum-enhanced metrology, *Nature Physics* **7**, 406 (2011).
- [104] W. Zhong, Z. Sun, J. Ma, X. Wang, and F. Nori, Fisher information under decoherence in bloch representation, *Phys. Rev. A* **87**, 022337 (2013).
- [105] D. T. Pegg and S. M. Barnett, Phase properties of the quantized single-mode electromagnetic field, *Phys. Rev. A* **39**, 1665 (1989).
- [106] C. Gerry and P. Knight, *Introductory Quantum Optics* (Cambridge University Press, 2004).
- [107] R. Landauer, Irreversibility and heat generation in the computing process, *IBM Journal of Research and Development* **5**, 183 (1961).
- [108] S. Lloyd, Quantum-mechanical maxwell’s demon, *Physical Review A* **56**, 3374–3382 (1997).
- [109] J. Ikonen, J. Salmilehto, and M. Möttönen, Energy-efficient quantum computing, *npj Quantum Information* **3**, 1 (2017).
- [110] S. Vuglar and J. Gea-Banacloche, Recycling of a quantum field and optimal states for single-qubit rotations, *Phys. Rev. A* **109**, 022439 (2024).
- [111] C. Catana and M. Guță, Heisenberg versus standard scaling in quantum metrology with markov generated states and monitored environment, *Phys. Rev. A* **90**, 012330 (2014).
- [112] F. Albarelli, M. A. C. Rossi, D. Tamascelli, and M. G. Genoni, Restoring heisenberg scaling in noisy quantum metrology by monitoring the environment, *Quantum* **2**, 110 (2018).
- [113] S. Zhou, A. G. Manes, and L. Jiang, Achieving metrological limits using ancilla-free quantum error-correcting codes, *Phys. Rev. A* **109**, 042406 (2024).
- [114] D. Layden, S. Zhou, P. Cappellaro, and L. Jiang, Ancilla-free quantum error correction codes for quantum metrology, *Physical Review Letters* **122**, 4 (2019).
- [115] E. M. Kessler, I. Lovchinsky, A. O. Sushkov, and M. D. Lukin, Quantum error correction for metrology, *Phys. Rev. Lett.* **112**, 150802 (2014).
- [116] A. Fujiwara and H. Imai, A fibre bundle over manifolds of quantum channels and its application to quantum statistics, *Journal of Physics. A, Mathematical and Theoretical* **41**, 18 (2008).
- [117] L. Viola and S. Lloyd, Dynamical suppression of decoherence in two-state quantum systems, *Physical Review A* **58**, 2733–2744 (1998).
- [118] G. A. Álvarez and D. Suter, Measuring the spectrum of colored noise by dynamical decoupling, *Phys. Rev. Lett.* **107**, 230501 (2011).
- [119] R. D. Gill and B. Y. Levit, Applications of the van trees inequality: A bayesian cramér-rao bound, *Bernoulli* **1**, 59 (1995).
- [120] M. Tsang, Ziv-zakai error bounds for quantum parameter estimation, *Physical Review Letters* **108**, 23 (2012).

Appendix A: Raw versus True Complexity

In Section III A we introduce the quantum Fisher information (QFI) as a metric quantifying the estimation precision of the QPE protocol. In general, in noisy quantum metrology [24, 103] the QFI can be empirically expressed as

$$F_N = N^2 e^{-f(N, \epsilon)} \quad (\text{A1})$$

for some function $f > 0$ that grows with both N and ϵ , characterising the information-destroying effect of the error. In the ideal limit, $\epsilon = 0$, we have $f(N, 0) \sim 1$ and we attain the Heisenberg limit for the sequential QPE protocol, $F_N \propto N^2$ [49, 83]. However, in the presence of noise, this scaling often cannot be realised in practice. In particular, for $f \sim \log(N)$ we reach the standard quantum limit, $F_N \sim N$, while, for even stronger implementation error, the QFI eventually decays as N grows, and adding more steps becomes detrimental for the estimation precision. The examples we study in this work correspond to the latter case; see Figure 2(a) and 9.

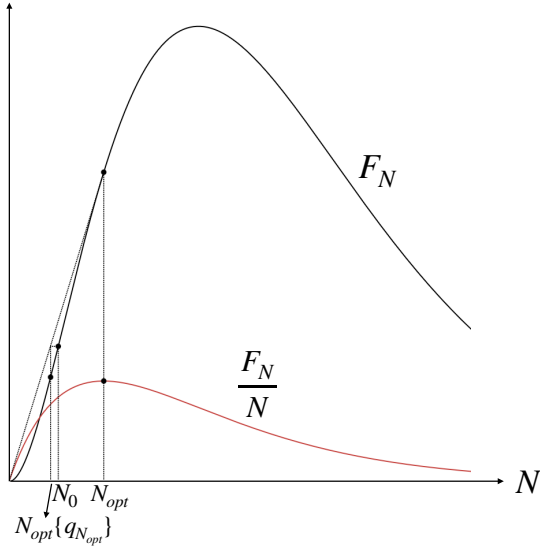


FIG. 8. Typical graph of the QFI F_N and its ratio with N for an asymptotically decaying QFI with respect to the number of steps N in one sequence. Initially, F_N increases quadratically while F_N/N increases linearly. Note that they attain their maximum at different values of N ; in particular, N_{opt} maximises F_N/N and leads to the raw complexity in Eq. (8). In the computation there, $N_{\text{opt}}\{q_{N_{\text{opt}}}\} < N_{\text{opt}}$ is taken to be the number of steps in the last sequence, while N_0 given by Eq. (9) is instead the true number of steps needed to reach the desired QFI. The discrepancy between the two is caused by the nonlinearity of F_N and is expected to decrease as the implementation error grows.

With the general qualitative form (A1), the difference between the raw and the true complexity becomes clearer to see. For N -step sequences, the raw complexity (8) is computed assuming the last partial sequence consists of $N \cdot \{q_N\}$ steps, where $\{q_N\}$ is the fractional part of q_N , while for the true complexity (10), the last sequence contains N_0 steps that satisfy the condition (9). In general, $F_{N\{q_N\}} \neq F_{N_0}$ unless F_N is linear over N , or when q_N is an integer (and so $N_0 = \{q_N\} = 0$). More precisely, we have

$$\frac{N\{q_N\}}{N} = \frac{F_{N_0}}{F_N} = \frac{N_0^2 e^{-f(N_0, \epsilon)}}{N^2 e^{-f(N, \epsilon)}} > \frac{N_0^2}{N^2},$$

and a rough upper bound on the difference between the actual length of the final sequence needed to reach the desired total QFI and the one as computed by the raw complexity is $N_0 - N\{q_N\} < N_0 - N_0^2/N \leq N/4$. These quantities are demonstrated in Figure 8 for a typical F_N with an eventual decay. Intuitively, as ϵ increases, the decaying of both F_N and F_N/N becomes faster and the turning point of the latter, N_{opt} , decreases. As the difference between the raw and the true complexity is upper bounded by roughly $N_{\text{opt}}/4$, and both supposedly increase with increasing error, we anticipate the true complexity to be well approximated by the raw complexity for large enough implementation error ϵ . This is confirmed by the observation made in Figure 2(b) and 4.

Appendix B: Computation of the Quantum Fisher Information F_N

To evaluate the QFI resulting from the implementation scheme in Section IV B, we first compute the action of the imperfect quantum channel. Recall Eqs. (11) and (12). Write a general qubit state in its Bloch representation, $\rho = \frac{1}{2}(\mathbf{I}_2 + \mathbf{s} \cdot \boldsymbol{\sigma})$, \mathbf{s} being the Bloch vector. From Eq. (18), the action of the implemented quantum channel on the state can be expressed as

$$\mathcal{G}_{\bar{m};g}(\rho) = \frac{\mathbf{I}_2}{2} + \frac{1}{2} \underbrace{\left(\int_0^{2\pi} \int_0^\infty \mathbf{R}_{\mathbf{n}} \left(g \sqrt{\frac{m}{\bar{m}}} \right) p(\theta) q(m) dm d\theta \right)}_{:= \mathbf{G}_{\bar{m};g}} \mathbf{s} \cdot \boldsymbol{\sigma},$$

where $\mathbf{n} = [\cos \theta, \sin \theta, 0]^\top$ and $p(\theta)$, $q(m)$ are the probability distributions followed by the phase and the photon number, respectively. The rotation matrix can be found through Rodrigues' formula: in general,

$$\mathbf{R}_{\mathbf{n}}(\alpha) = \mathbf{I}_3 + (\sin \alpha) \mathbf{N} + (1 - \cos \alpha) \mathbf{N}^2, \quad \mathbf{N} = \begin{bmatrix} 0 & -n_z & n_y \\ n_z & 0 & -n_x \\ -n_y & n_x & 0 \end{bmatrix}.$$

To assist with analytical derivation, we assume that the average photon number \bar{m} is large enough ($\gtrsim 100$) such that $p(\theta)$ and $q(m)$ are well-approximated by normal distributions:

$$q(m) = \frac{1}{\sqrt{2\pi\sigma_m^2}} e^{-\frac{1}{2}\left(\frac{m-\bar{m}}{\sigma_m}\right)^2}, \quad p(\theta) = \frac{1}{\sqrt{2\pi\sigma_\theta^2}} e^{-\frac{1}{2}\left(\frac{\theta}{\sigma_\theta}\right)^2},$$

σ_m and σ_θ being the corresponding variances. With these the integral can be computed to be

$$\mathbf{G}_{\bar{m};g} = \mathbf{I}_3 + \eta^{\frac{1}{4}} B \begin{bmatrix} 0 & 0 & 0 \\ 0 & 0 & -1 \\ 0 & 1 & 0 \end{bmatrix} + (1-A) \begin{bmatrix} -\frac{1-\eta}{2} & 0 & 0 \\ 0 & -\frac{1+\eta}{2} & 0 \\ 0 & 0 & -1 \end{bmatrix}, \quad \eta = e^{-2\sigma_\theta^2}, \quad (\text{B1})$$

where

$$A = \frac{\bar{m}}{\sqrt{2\pi\sigma_m^2}} \int_{-1}^{\infty} \cos(g\sqrt{1+t}) e^{-\frac{1}{2}\left(\frac{\bar{m}}{\sigma_m}\right)^2 t^2} dt, \quad B = \frac{\bar{m}}{\sqrt{2\pi\sigma_m^2}} \int_{-1}^{\infty} \sin(g\sqrt{1+t}) e^{-\frac{1}{2}\left(\frac{\bar{m}}{\sigma_m}\right)^2 t^2} dt.$$

In our case, the Bloch vector of the initial state, $|0\rangle\langle 0|$, is $\mathbf{s}_0 = [0, 0, 1]^\top$. Since $\mathbf{G}_{\bar{m};g}$ acts irreducibly on the yz plane, we may restrict dynamics to this subspace. The restricted Bloch vector after each step evolves as

$$\begin{aligned} \mathbf{s}_N &= (\mathbf{G}_{\bar{m};g})^N \mathbf{s}_0 \\ &= \begin{bmatrix} 1 - \frac{1}{2}(1-A)(1+\eta) & -\eta^{\frac{1}{4}} B \\ \eta^{\frac{1}{4}} B & A \end{bmatrix}^N \begin{bmatrix} 0 \\ 1 \end{bmatrix} \\ &= \frac{r^{N-1}}{\sin \alpha} \begin{bmatrix} -\eta^{\frac{1}{4}} B \sin(N\alpha) \\ A \sin(N\alpha) - r \sin((N-1)\alpha) \end{bmatrix}, \end{aligned} \quad (\text{B2})$$

where the two eigenvalues of $\mathbf{G}_{\bar{m};g}$ are expressed as

$$r e^{\pm i\alpha} = \frac{1}{4} \left(1 - \eta + A(\eta + 3) \pm i\sqrt{16\eta^{\frac{1}{2}} B^2 - (1-A)^2(1-\eta)^2} \right).$$

The state after the N^{th} step is $\rho_N = \frac{1}{2}(\mathbf{I}_2 + \mathbf{s}_N \cdot \boldsymbol{\sigma})$. From its Bloch representation, the QFI after the N^{th} step with respect to the parameter g can be readily calculated (see, for example, Ref. [104]):

$$F_N = \begin{cases} |\partial_g \mathbf{s}_N|^2 + \frac{(\mathbf{s}_N \cdot \partial_g \mathbf{s}_N)^2}{1-|\mathbf{s}_N|^2}, & |\mathbf{s}_N| < 1; \\ |\partial_g \mathbf{s}_N|^2, & |\mathbf{s}_N| = 1. \end{cases} \quad (\text{B3})$$

To continue the computation, we assume further that the light field has photon statistics corresponding to either a Poisson (coherent) or sub-Poisson distribution, such that $\sigma_m = k_m \sqrt{\bar{m}}$, $\sigma_\theta = \frac{k_\theta}{2\sqrt{\bar{m}}}$ with $k_m \sim \mathcal{O}(1)$. Then, for $\bar{m} \gg g^2$, various terms may be approximated as

$$\begin{aligned} A &\approx \sqrt{\frac{\bar{m}}{2\pi k_m^2}} \int_{-\infty}^{\infty} \cos\left(g\left(1 + \frac{t}{2}\right)\right) e^{-\frac{\bar{m} t^2}{2k_m^2}} dt = e^{-\frac{(gk_m)^2}{8\bar{m}}} \cos(g) \approx \left(1 - \frac{(gk_m)^2}{8\bar{m}}\right) \cos(g); \\ B &\approx \left(1 - \frac{(gk_m)^2}{8\bar{m}}\right) \sin(g); \quad \eta \approx 1 - \frac{k_\theta^2}{2\bar{m}}, \end{aligned}$$

leading to

$$\alpha \approx g, \quad r \approx 1 - \frac{\Delta(g)}{2\bar{m}}, \quad \Delta(g) = \frac{k_m^2 g^2 + k_\theta^2 (1 - \cos(g))}{4}.$$

Similarly, the Bloch vector (B2) and its derivative are

$$\mathbf{s}_N = r^N \left(\begin{bmatrix} 0 \\ -\sin(Ng) \\ \cos(Ng) \end{bmatrix} + \mathcal{O}\left(\frac{g^2}{\bar{m}}\right) \right), \quad \partial_g \mathbf{s}_N = r^N \left(-N \begin{bmatrix} 0 \\ \cos(Ng) \\ \sin(Ng) \end{bmatrix} + \mathcal{O}\left(\frac{g}{\bar{m}}\right) \right). \quad (\text{B4})$$

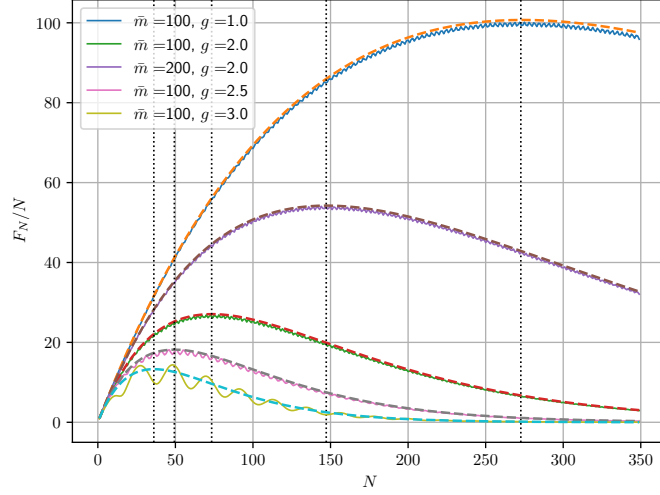


FIG. 9. Plots of F_N/N for various \bar{m} and g , when the field is in coherent states. Solid lines are the exact results using Eqs. (B2), (B3) and the dashed ones are the approximated ones (B5). The vertical dotted lines approximate the optimal step $N_{\text{opt}} = -[2 \log(r)]^{-1}$. As expected, the smaller and the larger g and \bar{m} are, respectively, the more negligible the percentage error becomes.

The leading order effect of $\mathbf{G}_{\bar{m},g}$ on the yz -plane is a rotation of angle g combined with a shrinking of factor r . This coincides with the phase-covariant channel (13) by identifying r with λ_{\perp} (and replacing the Z -basis with X -basis). Eq. (14) may thus be adopted to estimate the QFI, leading to

$$F_N(\bar{m}; g) = N^2 r^{2N} \left(1 + O\left(\frac{g}{\bar{m}}\right) \right) \approx N^2 \left(1 - \frac{\Delta(g)}{2\bar{m}} \right)^{2N}. \quad (\text{B5})$$

The merit of the approximation is confirmed by Figure 9 for coherent states.

Finally, the number-phase uncertainty relation states that $\sigma_m \sigma_{\theta} \geq \frac{1}{2}$ and so $k_m k_{\theta} \geq 1$ [105]. This implies the lower bound,

$$\Delta(g) \geq \frac{k_m k_{\theta} g \sqrt{1 - \cos(g)}}{2} \geq \frac{g \sqrt{1 - \cos(g)}}{2}, \quad (\text{B6})$$

with equality attained at $k_m = g^{-1/2} (1 - \cos(g))^{1/4} = k_{\theta}^{-1}$. A squeezed coherent state with real squeezing parameter s has $k_m = e^{-s}$, $k_{\theta} = e^s$ and so the QFI is maximised at $s = \frac{1}{2} \log\left(\frac{g}{\sqrt{1 - \cos(g)}}\right)$; notice this optimal squeezing level is dependent on the unknown parameter g . That said, in the main text we will set the control field to be in coherent states ($s = 0$ and $k_m = k_{\theta} = 1$ [106]) due to their near-classical properties and easier experimental preparation.

Appendix C: Further Remarks on Energy Cost

1. Cost of Discarding Subsystems

In Section IV A we set the energy cost E considered in this work to originate from energy conservation, and for each gate applied to the system qubit in the QPE protocol this cost amounts to $\bar{m}\hbar\omega \approx \bar{m}\hbar\omega_0$. Meanwhile, Landauer's principle [107, 108] states that the minimal energy cost of erasing information from one qubit is on the scale of $k_B T_0$, with T_0 being the system temperature. The relative magnitude between the two fundamental energy costs is then

$$\frac{E_{\text{conservation}}}{E_{\text{Landauer}}} \sim \frac{\bar{m}}{\xi}, \quad \xi = \frac{k_B T_0}{\hbar\omega_0}. \quad (\text{C1})$$

Using the value $\xi \approx 0.2$ as quoted in Section IV C 2 under typical experimental settings, one sees that, for the range of photon number $\bar{m} \gtrsim 100$ considered in our semi-classical approximation on the EM field, the energy cost from conservation as defined in

Eq. (15) is at least several orders of magnitude larger than the fundamental thermodynamic erasure cost arising from Landauer’s principle, justifying the omission of the latter in our analysis. This in particular validates our assumption in Table II that discarding ancillary qubits can be regarded as a free operation. As per the fundamental thermodynamic cost of discarding the field state after implementing each phase-encoding channel, note that the back-action on the field due to the field-qubit interaction (17) is small in our semi-classical regime, meaning that the post-evolution field state is still very close to a pure state (with vanishing temperature), and its discarding cost is consequently assumed to be negligible as well compared to the total energy of the field. In the following subsection, we briefly discuss how reusing or recycling the post-evolution field state may incur further energy savings.

2. Energy Saving Strategies

Here we qualitatively describe two possible generalisations to reduce the total energy cost, both of common practice. First, as shown in Appendix B, $\Delta(g)$ may be reduced according to Eq. (B6), if squeezing is introduced to the EM field. For a fixed \bar{m} this leads to a smaller complexity (see Eq. (21)), at the cost of extra squeezing energy per gate (the energy of a squeezed coherent state with real squeezing is $\bar{m} + \sinh^2(s)$). An energy-optimal squeezing level can be accordingly determined.

The energy cost can be further saved through field recycling. After the implementation of each channel, the field state is slightly entangled with the system qubit and its final (mixed) state will marginally deviate from the initial (pure) state, leading to larger implementation error for the next iteration if we reuse the final field state as it is. To circumvent such back-action — which, albeit small in each gate implementation, can accumulate significantly throughout the full QPE protocol — in the main text we completely reset the field after each phase-encoding gate is implemented. Note that this may also be the result of an operational constraint, where each query to the agent in charge of implementing the gate must be made independently and hence the implementation error at each step is uncorrelated from the previous history. Instead, we can imagine that some restoring procedure may be allowed to recycle the same field for the next step, hence saving the reinitialisation energy of the field. For example, as studied in Ref. [109, 110], consider a squeezed coherent state after interacting with the system qubit and slightly perturbed by the back-action. The original field state can be well restored by sequentially interacting the field with an additional ancilla qubit for some carefully tailored duration, through the free interaction (17). The more times the interaction is repeated, the closer the final field state will be to the original squeezed coherent state, and the smaller the implementation error will be for the next step, at the cost of larger ancilla overhead. This leads to another complexity versus (recycling) energy trade-off relation. The improvement may also be enhanced if monitoring is allowed on the field [111, 112]. A precise treatment on the energy reduction brought by more sophisticated field manipulation procedures is left to a later work.

3. Error Mitigation Controls

Although we aim to keep the current QPE protocol simple to demonstrate the qualitative behaviour of its energy cost from basic building blocks, it is interesting to investigate whether (in addition to varying the number of photons spent per gate) adding intermediate control operations on the probe system, as illustrated in Figure 10, may help improve the QPE performance.

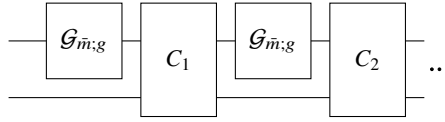


FIG. 10. A typical ancilla-assisted control sequence used to suppress the noise on the system qubit.

Recall the implemented channel, whose action on the Bloch sphere is described by Eq. (B4), can be approximated as the desired unitary operation U_g followed by a bit flip channel with flipping probability $p = \frac{1-r}{2} = \frac{\Delta(g)}{4\bar{m}}$:

$$\mathcal{G}_{\bar{m},g}(\rho) = (1-p)U_g\rho U_g^\dagger + p\sigma_x U_g\rho U_g^\dagger \sigma_x.$$

The goal of the control operations would then be to reduce the bit flip noise.

However, since in our case the noise generator σ_x coincides with the Hamiltonian that generates the signal, it is fundamentally impossible to isolate and suppress the noise. Indeed, results in Ref. [49] indicate that the QFI obtained in Eq. (19) is optimal within our sequential framework. Common error mitigation techniques, such as quantum error correction [28, 113–115], feedback controls [26, 29], and passive ancillae [24, 48, 116] cannot help increase the QFI; in other words, for our protocol

the best possible control operations C_1, C_2, \dots in Figure 10 all reduce to the identity. Further improvement is only possible if we introduce entanglement amongst probes of different sequences. We refrain from doing so since combining energy and entanglement, as two distinct resource quantities, demand a more careful bookkeeping on the total resource cost, a point brought up again in the concluding Section V.

The aforementioned error mitigation techniques nevertheless becomes effective when other types of noise take place — such as decoherence arising from system–environment interaction that does not commute with U_g ; common examples include dephasing and depolarisation [5]. If the field state is recyclable as described in Section C 2, the implementation errors at each step are correlated through the shared field (as well as other potential sources of memory effects from the environment) and the effective noise becomes non-Markovian, which can be suppressed e.g. through dynamical decoupling procedures [117, 118]. Even within the current scope, when the photon number \bar{m} is small enough, apart from the leading order bit flip noise, non-commuting terms also start to have a significant effect. Intuitively, we anticipate the appearance of yet another complexity versus (control) energy trade-off relation, where the error mitigation control increases the total QFI and hence reduce the complexity, while introducing extra energy cost for its implementation. A more thorough analysis on such an interplay will be explored in a forthcoming work.

Appendix D: Finite-Sample Effects on Estimator Variance

The sweet spot discovered in Section IV B corresponds to the regime where a single sequence suffices to reach the target total QFI, and hence the desired variance bound δ^2 implied by the quantum Cramér–Rao bound (QCRB) (6). While the QFI provides a well-established figure of merit, leading to a convenient and computable constraint when determining the complexity in Eq. (2), it does not automatically reflect the achievable estimation precision in the finite-sample regime. This is because, as remarked in the main text, the QCRB assumes an unbiased estimator from the optimal measurement, which in general only holds asymptotically when the sequence is repeated for a sufficiently large number of times, $Q \gg 1$, and adaptive strategies are implemented [13–15].

To assess the impact of finite-sample effects, one may consider alternative bounds on the estimator variance that do not rely on asymptotic or unbiasedness assumptions, such as the Bayesian generalisation of the Cramér–Rao bound based on the van Trees inequality [119]. In what follows, we focus on the quantum Ziv–Zakai bound (QZZB) as a universally valid lower bound that holds for any estimator bias [120] and is therefore applicable even in the single-shot regime $Q \sim 1$. Assuming a uniform prior distribution for g over an interval of width Γ and mean μ , the QZZB reads

$$\text{Var}[\hat{g}] \geq \frac{1}{2\Gamma} \int_0^\Gamma dx x \int_{\mu-\frac{\Gamma}{2}}^{\mu+\frac{\Gamma}{2}-x} dg \left[1 - \sqrt{1 - F(\rho_N(g), \rho_N(g+x))} \right], \quad (\text{D1})$$

where $F(\cdot, \cdot)$ is the quantum fidelity between two states and $\rho_N(g)$ is the final state after N steps, for a value g of the parameter to be estimated. For a qubit system, the fidelity between two states with Bloch vectors \mathbf{s}_1 and \mathbf{s}_2 is

$$F(\rho_1, \rho_2) = \frac{1}{2} \left(1 + \mathbf{s}_1 \cdot \mathbf{s}_2 + \sqrt{(1 - |\mathbf{s}_1|^2)(1 - |\mathbf{s}_2|^2)} \right).$$

In our setting, using Eq. (B4) for the Bloch vector and working in our usual semi-classical regime specified by $\bar{m} \gtrsim 10^2$, we can approximate the shrinking factor with the constant $r \approx 1 - \frac{\Delta(\mu)}{2\bar{m}}$. Under this approximation, the fidelity becomes independent of g and reads

$$F(\rho_N(g), \rho_N(g+x)) \approx 1 - r^{2N} \sin^2 \left(\frac{Nx}{2} \right).$$

Substituting into the QZZB (D1) we get

$$\text{Var}[\hat{g}] \gtrsim \frac{1}{2} \int_0^\Gamma dx x \left(1 - \frac{x}{\Gamma} \right) \left(1 - r^N |\sin(Nx/2)| \right).$$

For large $N \approx N_{\text{opt}}$, as done in Eq. (20), we use the approximation $r^N \approx e^{-1/2}$ and replace the oscillatory term by its average value, $|\sin(Nx/2)| \rightarrow 2/\pi$, obtaining

$$\text{Var}[\hat{g}] \gtrsim k\Gamma^2, \quad k = \frac{1 - \frac{2}{\pi\sqrt{e}}}{12} \approx 0.05. \quad (\text{D2})$$

This bound provides a finite-sample benchmark that can be compared with the asymptotic QCRB. For the QFI derived in the main text to reflect the achievable estimation precision, we require the QCRB (6) to be at least as informative as the QZZB bound

(D2). This is satisfied if, again using the derivation in Eq. (20),

$$\frac{1}{F_{N_{\text{opt}}}} \approx e \left(\frac{\Delta(\mu)}{\bar{m}} \right)^2 \gtrsim k\Gamma^2 \Rightarrow \Gamma \lesssim \frac{14.8}{\bar{m}},$$

for $\mu \approx 2.5$ as adopted in Figures 4, 5, 6. Therefore, a smaller \bar{m} allows for a less stringent demand on the prior knowledge on g , translating into a more informative QCRB in the finite-sample regime. Furthermore, recall that the constraint to determine the complexity (10) is a desired lower bound δ^2 on the estimator variance. Naturally, this bound should be at least tighter than the one given by the prior uniform distribution on g , meaning that $\delta^2 \lesssim \Gamma^2/12$, and thus

$$\bar{m} \lesssim \frac{4.3}{\delta}.$$

For our choice of $\delta^2 = 10^{-4}$ in the main text, this imposes a constraint on the photon number, $\bar{m} \lesssim 5 \cdot 10^2$.

Combining the above considerations, we identify a *Goldilocks regime*

$$10^2 \lesssim \bar{m} \lesssim 5 \cdot 10^2, \quad (\text{D3})$$

in which the assumptions underlying the analysis in the main text — most notably the semi-classical approximation — are satisfied and the QCRB remains an informative benchmark for the achievable estimation precision despite finite-sample effects. Consequently, the sweet spot identified in Section IV B yields a physically meaningful resource trade-off.

Overall, the analysis in this Section indicates that operating at smaller photon number per gate not only reduces the implementation energy, but also improves the consistency between finite-sample performance and the asymptotic precision benchmark.

Appendix E: Classical Fisher Information from Imperfect Measurements

Following from the pointer model introduced at the beginning of Section IV C 3, suppose we perform a measurement represented by the POVM $\mathbf{M} = (M_1, M_2) = (|0\rangle\langle 0|, |1\rangle\langle 1|)$ on the pointer state. If the pointer is initially in the pure state $|0\rangle\langle 0|$, then it can be checked that the corresponding POVM on the system qubit is exactly \mathbf{M} as desired. However, instead the pointer is prepared in a thermal state (32) after a dynamic cooling procedure as described in Section IV C 2. For simplicity we assume the cooling qubits are the same as those during the state preparation stage, although in the main text they may have different initial temperature and transition frequency depending on experimental realisation. The same measurement procedure now yields the modified POVM,

$$\tilde{\mathbf{M}} = (1 - \varepsilon)\mathbf{M} + \varepsilon\mathbf{N}, \quad \mathbf{N} = (M_2, M_1), \quad \varepsilon = \frac{1 - \gamma(T)}{2},$$

where $T \approx 2T_0/M_m$ and M_m is the number of qubits consumed to cool the pointer. Consequently, the estimation precision is reflected by the CFI (5) achieved by the non-optimal $\tilde{\mathbf{M}}$, rather than the QFI achieved by \mathbf{M} . To compute the effect of this imperfect measurement, we adopt the results from Ref. [82]. The susceptibility of the CFI with respect to a small disturbance on the POVMs is defined as

$$\chi[\mathbf{M}, \mathbf{N}] = \lim_{\varepsilon \rightarrow 0} \frac{F_c[\mathbf{M}] - F_c[\tilde{\mathbf{M}}]}{\varepsilon F_c[\mathbf{M}]}.$$

In our case, $F_c[\mathbf{M}] = F_N(\bar{m}; g)$. The CFI can be approximated up to the leading order of the perturbation ε as $F_c[\mathbf{M}] (1 - \varepsilon\chi[\mathbf{M}, \mathbf{N}])$. By plugging in Eq. (5) explicitly and using properties of the POVMs, this can be simplified to

$$F_N(\bar{m}; g) \xrightarrow{\text{measurement}} F_N(\bar{m}; g, \varepsilon) \approx F_N(\bar{m}; g) - (l_1 - l_2)^2 \varepsilon.$$

To compute $l_{1,2}$, recall that while extracting the leading order contribution to the QFI (B5), the Bloch vector of the probe state is approximated by Eq. (B4); in particular, $\mathbf{s}_N \cdot \partial_g \mathbf{s}_N \approx 0$. The SLD operator can then be easily guessed as $\Lambda_g = \partial_g \mathbf{s}_N \cdot \boldsymbol{\sigma} = 2\partial_g \rho_N$ (also see Ref. [104]). The POVMs that maximise the CFI are projectors onto the eigenspaces of Λ_g ,

$$M_i = \frac{\mathbf{I}_2 + \hat{m}_i \cdot \boldsymbol{\sigma}}{2}, \quad \hat{m}_i \approx \pm \frac{\partial_g \mathbf{s}_N}{|\partial_g \mathbf{s}_N|},$$

leading to

$$(l_1 - l_2)^2 \approx \left(\frac{\partial_g \mathbf{s}_N \cdot \hat{m}_1}{\underbrace{1 + \mathbf{s}_N \cdot \hat{m}_1}_{=0}} - \frac{\partial_g \mathbf{s}_N \cdot (-\hat{m}_1)}{1 + \mathbf{s}_N \cdot (-\hat{m}_1)} \right)^2 = 4|\partial_g \mathbf{s}_N|^2 \approx 4F_N(\bar{m}; g),$$

where the last relation comes from Eq. (B3). Therefore, the CFI with the measurement error taken into account is simplified to $(1 - 4\varepsilon)F_N(\bar{m}; g)$.

Combined with Eq. (33), the overall modification to the QFI due to non-ideal state preparation and measurement is

$$F_N(\bar{m}; g) \xrightarrow{\text{state preparation + measurement}} F_N(\bar{m}; g, M_s, M_m) \approx \left[\gamma \left(\frac{2T_0}{M_s} \right) \right]^2 \left[2\gamma \left(\frac{2T_0}{M_m} \right) - 1 \right] F_N(\bar{m}; g). \quad (\text{E1})$$

The resulting complexity and total energy cost can be derived in the same fashion as in Section IV C 2.